Simulation of Argon Gas Flow Effects in a Continuous Slab Caster

B.G. THOMAS, X. HUANG, and R.C. SUSSMAN

Three-dimensional finite-volume-based numerical models of fluid, heat, and mass transport have been developed and applied to help explain the complex inter-related phenomena of multiphase fluid flow, superheat dissipation, and grade intermixing during the continuous casting of steel slabs. Gas bubbles are simulated using a continuum model, which calculates the volume fraction and velocities of the gas, and its effect on the liquid flow. Turbulence has been incorporated using the standard K-ε turbulence model. Reasonable agreement has been achieved between predicted velocities and corresponding measurements and observations in full-scale water models, both with and without gas injection. The effects of argon gas bubble injection on flow-related phenomena are investigated with simulations of a typical steel slab caster. Argon bubbles alter the flow pattern in the upper recirculation zone, shifting the impingement point and recirculation zones upward. The effect increases with increasing gas fraction and decreasing bubble size. Argon injection also causes superheat to be removed higher in the caster, moves the hot spot upward, lowers the peak heat flux, and increases heat extraction from the wide face and meniscus regions. During a steel grade transition, argon injection slightly affects slab surface composition but has no effect on intermixing in the slab interior.

I. INTRODUCTION

ARGON gas is employed at several stages in the continuous casting process (ladle, tundish, and mold) to encourage mixing, to help prevent nozzle clogging, and to promote the flotation of solid inclusion particles from the liquid steel. It usually enters the continuous casting mold after injection into the submerged entry nozzle (SEN), and eventually escapes from the liquid steel surface through the mold flux powder layer.

Argon injected into the SEN provides a positive pressure inside the nozzle, which inhibits the natural aspiration of air through cracks, pores, or joints in the nozzle walls, such as the junction between the nozzle and sliding-gate flow-metering plates. This helps to prevent the formation of the associated reoxidation products, such as alumina, which otherwise form detrimental solid inclusions that can adhere to the nozzle walls to block the flow of liquid or enter the mold cavity with the steel to create other quality problems. Argon helps to prevent nozzle clogging in a second way by creating turbulence that discourages adherence of inclusions to the nozzle walls. Once inside the mold cavity, the argon bubbles are believed to preferentially attach with inclusion particles, thus promoting their removal when the argon leaves the surface of the liquid pool.

In addition to these beneficial effects, argon can have detrimental side effects. Gas bubbles, and their associated clusters of attached inclusions, may become trapped in the solidifying shell and create serious defects just beneath the slab surface. Alternatively, they may disturb the liquid steel surface when they exit the powder layer, generating detrimental surface turbulence and consequent surface defects. These effects are influenced by the amount and size of the argon bubbles and the flow pattern inside the mold cavity. Moreover, the injected argon gas bubbles also influence this flow pattern. In addition, this has corresponding effects on the extraction of superheat, composition intermixing during a grade transition, and the movement of solid inclusion particles. The extent of these effects is intensified by the volume expansion of the gas bubbles in the high-temperature molten steel. These effects have not been quantified previously, and they are the focus of the present modeling study.

B.G. THOMAS, Associate Professor, and X. HUANG, Postdoctoral Research Associate, are with the Department of Mechanical and Industrial Engineering, University of Illinois at Urbana–Champaign, Urbana, IL 61801. R.C. SUSSMAN, General Manager of Process Research, is with Armco, Inc., Middletown, OH 45043.

Manuscript submitted July 6, 1993.

II. PREVIOUS WORK

Experimental measurements on an operating continuous casting machine are very difficult, dangerous, and expensive. Multiphase flow phenomena, particularly volumetric expansion of the gas, are also difficult to simulate using physical water models. The recent development of numerical modeling provides an alternative tool for understanding and solving this kind of problem in material processing. Several mathematical models have been applied to argon-steel flow and its associated heat and mass transfer in gas-agitated vessels, such as casting ladles.[1–11] Research efforts have also been dedicated to the fundamentals of gas-liquid flow dynamics and behavior of bubbles and bubble plumes, both with mathematical models[12–15] and with physical models using hot liquid metals (liquid iron, steel, and copper)[16,17] and other liquids such as water, mercury, liquid silver, butanol solute, aqueous glycerol, and ethyl alcohol.[12–15,17–24]

Relatively little work has been reported on two-phase flow in the continuous casting mold. One of the few studies, by Bessho *et al.*,[25] compared the calculated

flow pattern, gas holdup (volume fraction), and inclusion distribution in a full-scale water model with experimental measurements and observations. Although only one case was reported, the results showed that gas created a great change in the flow pattern. A water modeling study observed the dependence of bubble penetration depth on nozzle design.[26] The authors concluded that bubble dispersion can be controlled by nozzle submergence depth and nozzle geometry, such as nominal port angle. However, the effect of gas bubbles on the flow was not investigated directly. Another water modeling study, by Andrzejewski *et al.*,[27] found that carefully controlled argon injection and submergence depth were able to improve flow in a wide mold and even reduce surface-flow velocity and level fluctuations.

The present work describes the development of three-dimensional (3-D) finite-volume models of two-phase flow of liquid steel with argon gas bubbles and its associated heat and mass transfer in the continuous slab casting mold. After verification with water models, the models are applied to investigate the effects of bubble size and injection rate on the flow pattern, superheat extraction, and intermixing during a steel grade transition. In later work, the model will be extended to simulate the movement of inclusion particles.

The transient nature of flow in the mold, which causes problems such as surface turbulence, is known to be very important to steel quality. However, as a first step toward understanding this complex behavior, the present work assumes a steady-state flow pattern and investigates the influence of argon gas injection on this flow pattern and related phenomena.

III. GAS-LIQUID FLOW MODEL

A. *Governing Equations*

A finite-volume-based numerical model has been developed to simulate 3-D two-phase (gas-liquid) flows, using the computational domain and grid of 60 × 34 × 16 nodes shown in Figure 1. Twofold symmetry is assumed, so only one quarter of the mold is modeled. The buoyancy force acting on the liquid because of the gas bubbles was taken into account by adding an extra force term, f_{gz}, into the momentum equation for the liquid phase in the vertical direction, z. The liquid velocities, v_i ($v_i = \{v_x, v_y, v_z\}$), and pressure, p, are defined by the 3-D, incompressible, steady-state, mass and momentum conservation equations for a Newtonian fluid:

$$\frac{\partial v_i}{\partial x_i} = 0 \qquad [1]$$

$$\rho v_j \frac{\partial v_i}{\partial x_j} = -\frac{\partial p}{\partial x_i} + \frac{\partial}{\partial x_j}\left[\mu_{\text{eff}}\left(\frac{\partial v_i}{\partial x_j} + \frac{\partial v_j}{\partial x_i}\right)\right] + \rho f_i + \rho f_{gi} \qquad [2]$$

where i and $j = \{1, 2, 3\} = \{x, y, z\}$ and $\{x_1, x_2, x_3\} = \{x, y, z\}$ in the Cartesian system; f_{gi}, as described above, is the extra force acting on the liquid due to buoyancy of the gas bubbles:

$$f_{gx} = 0, \qquad f_{gy} = 0, \qquad f_{gz} = -\sigma_g g \qquad [3]$$

and f_i are body forces which include only gravity in this work:

$$f_x = 0, \qquad f_y = 0, \qquad f_z = g \qquad [4]$$

The Reynolds number in the caster, based on the hydraulic diameter (Table I), always exceeds 10,000 even far below the mold. This indicates that the flow is highly turbulent everywhere. Thus, the standard K-ε turbulence model is used to calculate velocities of the liquid phase:

$$\mu_{\text{eff}} = \mu_0 + \mu_t \qquad [5]$$

$$\mu_t = c_\mu \rho \frac{K^2}{\varepsilon} \qquad [6]$$

$$\rho v_j \frac{\partial K}{\partial x_j} = \frac{\partial}{\partial x_j}\left(\frac{\mu_t}{\sigma_K}\frac{\partial K}{\partial x_j}\right) + \rho G_K - \rho\varepsilon \qquad [7]$$

$$\rho v_j \frac{\partial \varepsilon}{\partial x_j} = \frac{\partial}{\partial x_j}\left(\frac{\mu_t}{\sigma_\varepsilon}\frac{\partial \varepsilon}{\partial x_j}\right) + c_1 \frac{\varepsilon}{K}\rho G_K - c_2 \frac{\varepsilon}{K}\rho\varepsilon \qquad [8]$$

where

$$G_K = \frac{\mu_t}{\rho}\frac{\partial v_j}{\partial x_i}\left(\frac{\partial v_i}{\partial x_j} + \frac{\partial v_j}{\partial x_i}\right) \qquad [9]$$

$$c_1 = 1.44, \qquad c_2 = 1.92, \qquad c_\mu = 0.09,$$

$$\sigma_K = 1.0, \qquad \sigma_\varepsilon = 1.3 \qquad [10]$$

Bubble dispersion in the gas-liquid mixture due to turbulent transport and diffusion is modeled by the following transport equation for the continuum gas bubble concentration, σ_g:

$$v_{gj}\frac{\partial \sigma_g}{\partial x_j} = \frac{\partial}{\partial x_j}\left(D_g \frac{\partial \sigma_g}{\partial x_j}\right) \qquad [11]$$

where the diffusivity of gas bubbles in the mixture, D_g, is assumed to be equal to the turbulent diffusivity of a solute element with turbulent Schmidt number, Sc_t, set to 1; *i.e.*,

$$D_g = \frac{\mu_t}{\rho \text{Sc}_t} = \frac{\mu_t}{\rho} \qquad [12]$$

No momentum equation is solved for the low-density gas phase. Instead, the bubbles are assumed to have reached their steady-state terminal velocity in the vertical direction relative to the liquid phase, v_{gt}, by the time they have entered the domain of the mold cavity. The three components of gas velocity are thus simply

$$v_{gx} = v_x \qquad [13]$$

$$v_{gy} = v_y \qquad [14]$$

$$v_{gz} = v_z - v_{gt} \qquad [15]$$

The gas bubbles are assumed to be spheres with a uniform size, whose terminal velocity is found according to an empirical correlation[28] developed for large individual air bubbles rising in water:

$$v_{gt} = \exp(a_0)\exp(a_1 \ln d_g)\exp[a_2 (\ln d_g)^2] \qquad [16]$$

$$a_0 = -8.373, \quad a_1 = -2.6306, \quad a_2 = -0.2500 \qquad [17]$$

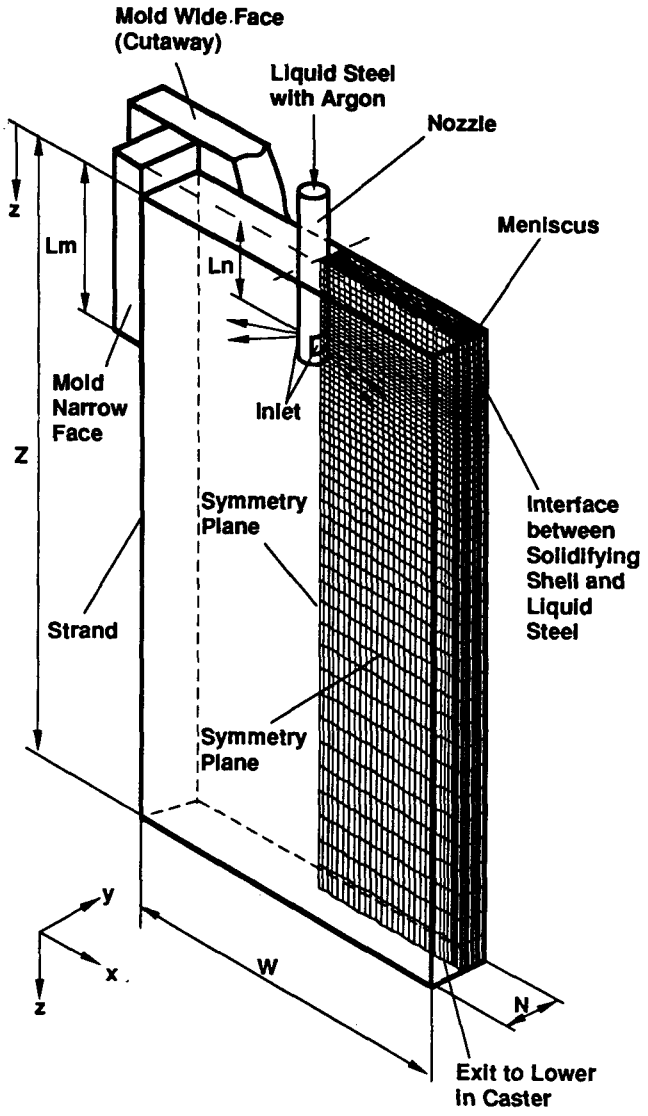

Fig. 1—Simulation domain and typical mesh used in 3-D steel-argon two-phase flow model.

B. *Boundary Conditions*

1. *Liquid phase*

Inlet boundary conditions, including jet angle, velocity profile, turbulent kinetic energy and its dissipation rate, are specified according to output from a separate 3-D finite-element model of the nozzle, described elsewhere.[29,30,31] The inlet, shown in Figure 1, represents the plane between the nozzle port and the mold cavity. To simplify its geometry in the present mold model, a rectangular inlet area is adopted for both rectangular and circular nozzle ports.

Because fluid always flows out through the bottom portion of the nozzle outlet port, and there is a small inward flow near the top portion,[29,30,31] the submergence depth used in the mold simulation refers to the distance from the top surface of the mold to the top of the jet, which is at the top of the inlet. This explains the greater jet submergence depths, L_n, employed to simulate the corresponding experiments, L_0. The distance between the top surface and the position of the maximum outflow from the nozzle is chosen to be the same in the simulation and the experiments.

For the outlet of the computational domain, which is a horizontal plane across the steel caster, and holes in the bottom of a physical water model, the normal gradients ($\partial/\partial n$) of all variables, including v_x, v_y, v_z, K, ε, and p are set to zero. The same boundary conditions are used for each node on a symmetry centerplane, except that the velocity component normal to the symmetry plane is set to zero. The top surface is treated the same as a symmetry plane, and the small variations in the liquid level due to motion of the free surface are neglected.

The bottom of the physical water model domain is simplified to make it symmetrical. The bottom of the standard water model, case A1 in Table I, was modeled with four holes in the symmetric half of the domain instead of four holes on just one side, as used in the experiments. This simplification is reasonable because it should have just a tiny effect on the flow only near the outlet holes, and flow asymmetry was not observed in the physical water model.

Empirical "wall law" functions[32] are employed to define the tangential velocities, K and ε, at the near-wall grid nodes in order to account for the steep gradients that exist near the walls.[33] When simulating steel casters, the domain extends up to, but does not include, the mushy zone or the solid shell. This avoids the computational difficulties associated with applying wall functions and modeling latent heat evolution at an internal solid/liquid interface. The boundaries of the mesh along the narrow and wide face walls correspond to the dendrite tips forming the outer limit of the mushy zone. These boundaries are treated as very rough solid walls by reducing the roughness factor in the wall laws from 8.8 to 0.8.[31] The validation of this approach of handling the computational domain has been addressed in previous work.[30,33,34]

2. *Gas phase*

A zero-gradient condition of gas bubble volume fraction, σ_g, is set for all boundaries except the inlet of the domain. This condition is consistent with no gas flow through the walls, while it allows gas to leave from the top surface, at the imposed relative terminal velocity. Gas could also be carried from the bottom of the domain, if the terminal velocity did not greatly exceed the casting speed.

C. *Gas Bubble Size and Volume Fraction at Mold Inlet*

Gas bubble size and volume fraction are very important input parameters which control bubble behavior in the flow simulation. Both of these parameters change significantly after injection into the liquid steel in the SEN as a result of both heating by the liquid steel and pressure variation. In this work, a simple formula was derived to calculate gas bubble size at the mold inlet plane, d_g, by applying the ideal gas state equation and assuming bubbles are injected at standard conditions (temperature 25 °C and pressure 1 atm):

Table I. Simulation Conditions for Flow Model

	Case A1 (51-mm × 76-mm Rectangular Port, Armco)	Case A2* (51-mm × 89-mm Rectangular Port, Armco)	Case A3* (51-mm Circular Port, Armco)	Case B1 (Long Model Inland)	Case B2** (Short Model Inland)	Case C (Steel Caster)
L_w (mm)	51			60		60
L_n (mm)	66	46	36	38		38
α_0 (°)	15 down		25 down	15 down		15 down
α (°)	25 down			25 down		24 down
L_n (m)	0.1828		0.1778	0.265		0.265
L_0 (m)	0.1524			0.235		0.235
Z (m)	2.152			3	1.12	3
W (m)	1.93			1.32		1.32
N (m)	0.229			0.22		0.22
V_c (m/s)	0.0152			0.0167		0.01667
E	8.8			8.8		0.8
μ_0 (N s/m^2)	0.001			0.001		0.0055
ρ (kg/m^3)	1000			1000		7020
v_{x0} (m/s)	1.048	1.513	1.908	1.062		1.062
v_{y0} (m/s)	0	0	0	0		0
v_{z0} (m/s)	0.489	0.672	0.848	0.427		0.471
K_0 (m^2/s^2)	0.0502	0.0281	0.0702	0.054		0.0502
ε_0 (m^2/s^3)	0.457	0.705	1.335	0.447		0.457
Gas	helium	none	none	none	air	argon
Q_g (m^3/s)	0, 0.00022	0	0	0	0.00026	0, 0.00012, 0.00026
σ_{g0} (pct)	0, 3 pct	0	0	0	5 pct	0, 11, 22 pct
d_{gi} (mm)	1, 5	none	none	none	1	0.6, 1.7, 3
d_g (mm)	1, 5	none	none	none	1	1, 3, 5

*Unlisted values are the same as case A1.
**Unlisted values are the same as case B1.

$$d_g = d_{gi}\left(\frac{\rho_{gi}}{\rho_g}\right)^{1/3} \quad [18]$$

$$\frac{\rho_{gi}}{\rho_g} = \left(\frac{P_\infty}{P_\infty + \rho g L_n}\right)\left(\frac{T_0 + 273}{T_\infty + 273}\right) \quad [19]$$

where ρ_{gi} and ρ_g are the gas densities at the injection point and the nozzle port, respectively; P_∞ is the ambient pressure (1 atm). The bubble temperature at the mold inlet is set to that of the liquid steel in derivation of Eq. [19] because the bubbles heat very quickly, as shown in the Appendix. It should also be noted that pressures at the flow meter and at the injection point in the SEN are likely to be higher.

Next, applying a mass balance on the gas flow through the system, the gas volume fraction at the mold inlet plane, σ_{g0}, can be obtained:

$$\sigma_{g0} = \frac{Q_g \dfrac{\rho_{gi}}{\rho_g}}{Q_g \dfrac{\rho_{gi}}{\rho_g} + V_c NW(1 - \sigma_{g\,\mathrm{out}})} \quad [20]$$

Equations [18] through [20] are used to determine the bubble size and gas volume fraction at the mold inlet of the steel caster, given the initial bubble size, d_{gi}, and volume flow rate, Q_g, and assuming the outlet volume fraction, $\sigma_{g\,\mathrm{out}}$, is negligible. For water model simulations, the density remains constant, so the gas bubble size remains constant, and the volume fraction from Eq. [20] simplifies.

D. *Solution Method*

Owing to the simple rectangular geometry of the mold, a computer code based on finite-difference calculations, MUPFAHT[35] has been chosen for this complex problem. The steady-state (elliptic) system of differential equations and boundary conditions is discretized into finite-difference equations using a staggered grid and seven-point stencil of control volumes. To aid convergence, an upwinding scheme is employed for the advection terms in domains with high cell Reynolds number.[36] In addition, the source terms are linearized to increase diagonal dominance of the coefficient matrix.[36] The equations are solved with the semi-implicit method of pressure-linked equations algorithm, whose alternating-direction-semi-implicit iteration scheme consists of three successive tri-diagonal-matrix-algorithm solutions (one for each coordinate direction) followed by a pressure-velocity modification to satisfy the mass conservation equation.[36]

Obtaining reasonably converged velocity and turbulence fields for this problem is difficult because of the high degree of recirculation. The current strategy employed is successive iteration using an under-relaxation factor of 0.2 or 0.3 until the maximum relative residual error and maximum relative error between successive solutions fall below 0.1 pct. Based on this criterion and starting from an initial guess of zero velocity, over 2500 iterations are required to achieve a converged solution. This takes about 20 CPU hours on a Silicon Graphics 4D/35 workstation for a mesh of 60 × 34 × 16.

IV. HEAT-TRANSFER MODEL FOR SUPERHEAT DISSIPATION

The dissipation of the superheat has an important influence on growth of the shell during the critical initial

stages of solidification. It also has an important effect on surface defect formation and steel internal quality related to the microstructure. To investigate superheat dissipation in the continuous slab casting mold, a heat-transfer model has been developed to compute temperature distribution within the liquid pool, heat transfer to the inside of the solidifying shell, and its effect on growth of the shell. This model solves a 3-D energy conservation equation:

$$\rho C_p\left(v_j\frac{\partial T}{\partial x_j}\right)=\frac{\partial}{\partial x_j}\left(k_{\text{eff}}\frac{\partial T}{\partial x_j}\right) \qquad [21]$$

Because conductive heat transfer is enhanced greatly by turbulent eddy motion, the effective thermal conductivity, k_{eff}, consists of two components:

$$k_{\text{eff}}=k_0+\frac{C_p\mu_t}{\text{Pr}_t} \qquad [22]$$

k_{eff} depends greatly on the turbulence parameters through the calculated turbulent viscosity, μ_t, and the turbulent Prandtl number, Pr_t, which is set to the standard value of 0.9 in the present work.[30,32]

A. *Boundary Conditions*

Temperature across the inlet plane is simply fixed to the casting temperature, T_0. This temperature corresponds to a tundish temperature, because the temperature drop through the nozzle is very small.[37] Adiabatic conditions or zero normal temperature gradient conditions ($\partial T/\partial n$) are used at the outlet plane and the symmetry centerplanes. For the top surface, calculations were made to estimate heat conduction through the molten flux and powder layers and radiating to ambient.[31] To account for this heat loss, an equivalent thermal convection boundary condition is applied to the top surface, using the heat-transfer coefficient, h, and ambient temperature, T_∞.

To correspond with the flow boundary conditions, the boundaries of the computational domain for heat transfer are again assumed to be the dendrite tips, so the domain does not include the solidified shell and the mushy zone. A fixed temperature, nominally equal to the liquidus, T_{liq}, is imposed along these boundaries. The reduction of the domain due to the solidification is neglected because the solidifying shell is very thin in the mold region.

An empirical "thermal wall law"[33] is used to determine temperature at the near-wall grid nodes. Use of this thermal wall function was important to achieve an accurate heat balance. It is needed to calculate the heat flux due to superheat dissipation, q_{sh}, which in turn influences the growth of the solidifying steel shell.

This approach differs from other recent models, which couple the fluid-flow and solidification calculations. The latter models use a function (based on flow through porous media) to radically reduce velocity and turbulence levels within the mushy zone.[38] By separating the fluid-flow and solidification calculations, the present approach reduces the complexity needed in subsequent models of heat conduction and solidification of the shell. Results from the present model have been incorporated into a thermal stress and shrinkage model that includes coupled heat flow across the mold/shell gap.[39]

B. *Incorporation of Gas Bubbles*

Argon gas bubbles influence heat transfer in the caster in two ways: by altering thermal convection through their effect on flow velocities, and by enhancing turbulent heat conduction by increasing turbulence intensity. This effect of gas on heat transfer has automatically been taken into account through the two-phase flow model described in Section III.

C. *Solution Methodology*

The differential equations, together with the boundary conditions described in Section A, were solved with the same finite-difference schemes used for the flow models. Because heat transfer has negligible effect on the fluid flow, (*i.e.*, there is only one-way coupling between the fluid-flow and heat-transfer models), previously converged solutions of the velocity and turbulence fields are input and kept unchanged during the solution of the temperature. Thus, only 30 minutes CPU time is needed on the Silicon Graphics 4D/35 workstation.

V. MASS-TRANSFER MODEL FOR GRADE TRANSITION

A 3-D transient mass-transfer model, consisting of three submodels, has been developed to calculate intermixing in both the strand and the solidified slab during a transition in steel grade.[40] The results presented in this work correspond to a "flying tundish change," where the steel grade is changed simultaneously with the ladle and tundish. The influence of argon gas bubble injection on mass transfer is automatically introduced through its effect on the time-averaged velocities, as done with heat transfer.

A. *3-D Transient Mass-Transfer Model of Upper Strand*

The first submodel calculates 3-D transient turbulent mass transfer of solute in the upper 6 m of the strand by solving the 3-D transient transport equation

$$\frac{\partial C}{\partial t}+v_j\frac{\partial C}{\partial x_j}=\frac{\partial}{\partial x_j}\left(D_{\text{eff}}\frac{\partial C}{\partial x_j}\right) \qquad [23]$$

where C is the dimensionless composition, or "relative concentration," defined by

$$C\equiv\frac{F(x,y,z,t)-F_{\text{old}}}{F_{\text{new}}-F_{\text{old}}} \qquad [24]$$

and $F(x,y,z,t)$ is the fraction of a given element at a specified position in the strand or slab; F_{old} and F_{new} are the desired fractions of that element in old and new grades respectively; D_{eff} is the effective diffusivity given by

$$D_{\text{eff}}=D_0+\frac{\mu_t}{\rho\text{Sc}_t} \qquad [25]$$

The initial value of C is set to zero throughout the domain to start the simulation. A sudden transition from $C = 0$ to $C = 1$ is imposed at the inlet plane, (which defines $z = 0$ in the final slab). Zero-gradient or "no mass diffusion" boundary conditions were applied to the composition at all other boundaries. Thus, solute can only leave the domain by fluid transport across the outlet plane.

B. *1-D Mass Transfer Model of Lower Strand*

Composition evolution must be calculated within the entire liquid pool of the strand (usually 20 to 40 m to the metallurgical length) before it is possible to predict the complete composition distribution in the final slabs. Fortunately, the 3-D results for the top 6 m indicate that the velocity profile in the lower region of the strand (below 6 m) is quite uniform and close to that of turbulent flow through a duct. Thus, for economy, a 1-D mass-transfer model of Eq. [23] in the z direction was developed as the second submodel, to simulate the remaining domain beyond 6 m.

C. *Slab Composition Model*

Composition distribution in the final slab develops as the solidifying shell grows in thickness down the caster. The third submodel calculates the composition distribution in the final slab from the 3-D time-varying concentration history of the strand, generated by the first two submodels. Composition at each point in the strand is assumed to evolve according to the calculated history until that point solidifies. Diffusion in the solid and macrosegregation are ignored. Mathematically, this model performs a coordinate transformation on the strand results, C, to obtain the composition in the final slab, C_{slab}:

$$C_{slab}(x_s, y_s, z_s) = C(x, y, z, t) \qquad [26]$$

where the spatial and time coordinates in the strand, x, y, z, and t, are related to the coordinates in the final slab, x_s, y_s, z_s, through the following equations:

$$x = x_s, \quad y = y_s, \quad z = \int_0^{t_s} v_z dt, \quad t = \int_{z_s}^{z} \frac{dz}{v_z} \qquad [27]$$

In the preceding equations, t_s represents the solidification time of the steel shell, which defines the depth (z distance) beneath the strand surface where the composition no longer changes. To specify t_s, a simple relationship involving x-y position in the strand, shell thickness, ΔL, and solidification constant, k_{shell}, was adopted:

$$t_s = \left(\frac{\Delta L}{k_{shell}}\right)^2, \qquad \Delta L = \min\left(\frac{W}{2} - y, \quad \frac{N}{2} - x\right) \qquad [28]$$

D. *Solution Method*

Like the solution procedure for the heat-transfer model, the 3-D and 1-D transient transport equations are solved after first obtaining the velocities and turbulence properties with the flow model. The solution method employs a backward Eulerian iteration within each variable-size time-step. A simulation of 960 seconds of casting requires about 50 time-steps and 8 hours of CPU time on the Silicon Graphics 4D/35 workstation. Further details are provided elsewhere.[40]

VI. TYPICAL MODEL FLOW RESULTS

The 3-D numerical model of two-phase flow, described in Section III, can simulate flow in either the actual steel slab continuous casting machine, or in a physical water model of the process, by making simple changes in the domain outlet boundary conditions, the liquid properties, and other conditions as desired. This section presents typical predictions of the flow pattern in a 2.15-m-high water model, for conditions A1 in Table I. The results are later compared with observations and measurements in the physical water model. The post-processor FIPOST, of the commercial finite-element program FIDAP,[41] was used to visualize and plot the results.

A. *Typical Flow Predictions in Water Model without Gas Injection*

Figure 2 illustrates the typical 3-D flow pattern predicted numerically for a water model with no gas injection. The actual water model will be described in the Section VII. For clarity of presentation, a velocity vector is drawn only at every eighth node in the grid. Figure 2(a) views the centerplane section parallel to the wide face wall. The fluid leaves the nozzle as a strong jet, impinges upon the narrow face, then splits vertically to create upper and lower recirculation regions. Figure 2(b) reveals the interior velocity vectors in transverse sections taken at five locations down the mold. Because the bifurcated nozzle sends flow into a relatively thin mold cavity, the resulting velocities are relatively uniform through the thickness of the mold over most of the mold interior. Down the corner near the impingement point, a weak vortex is formed, as the jet spreads across the narrow face and meets the incoming flow just off the corner along the wide face surface. Velocity components through the mold thickness are quite small everywhere except very near the outlet holes. Thus, flow in the mold can be characterized by the angle of the jet traversing the mold, the location of its impingement point on the narrow face, and by the location in the x-z plane of the centers of the recirculation zones: the "lower eye" and "upper eye." These flow parameters are illustrated in Figure 3.

B. *Typical Flow Predictions in Water Model with Gas Injection*

The influence of gas bubbles on the flow pattern is seen in Figures 3(b) and 4 for a uniform gas bubble size, d_g, of 1-mm diameter and a gas volume fraction at the inlet plane to the mold cavity, σ_{g0}, of 3 pct. The buoyancy of the gas bubbles changes the flow pattern significantly in the upper region of the mold, even for this small amount of gas injection. When the bubbles are

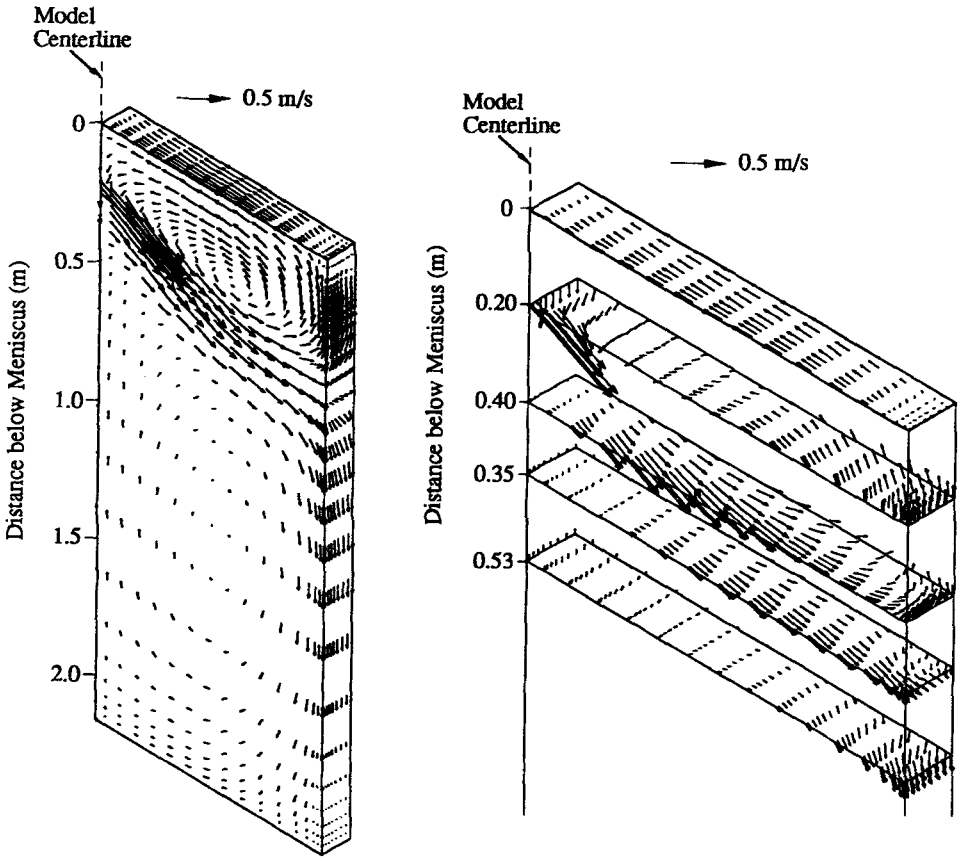

(*a*) 3-D view of velocity vectors.

(*b*) Velocity vectors in transverse sections down water model.

Fig. 2—Predicted flow patterns in water model (case A1 in Table I without gas).

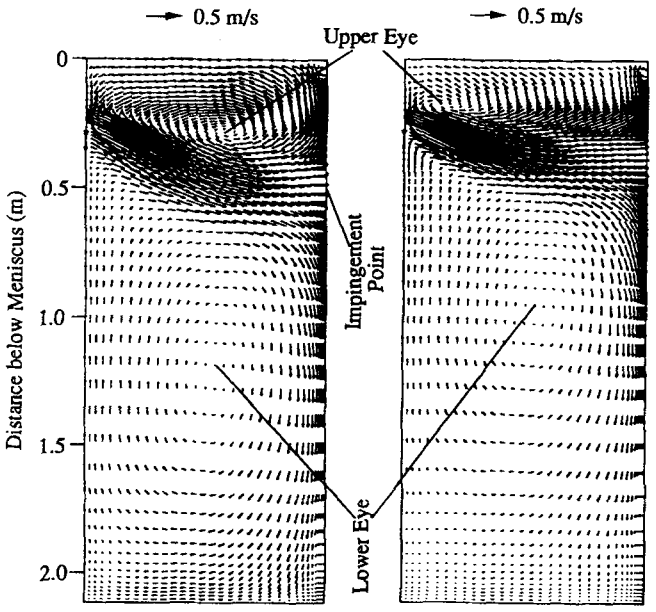

(*a*) No gas.

(*b*) With gas (bubble size 1 mm, 3% gas at inlet).

Fig. 3—Two-dimensional view of predicted flow patterns in water model (case A1 in Table I).

small, as assumed here, they travel with the jet and induce it to bend upward to impinge at a slightly higher location on the narrow face wall. This upward motion due to the bubbles is predicted to shift the location of the upper eye greatly toward the mold center and slightly upward to just above the nozzle port.

As the bubble-rich liquid in the central portion of the jet rises vertically, velocity gradients are created through the mold thickness. This effect is seen most clearly by comparing the 0.20-m slices in Figures 2(b) and 4. A large horizontal recirculation region is evident, so there is no unique location of the upper eye (Figure 4). As the rising bubble-rich liquid reaches the top surface, it slows down the flow of liquid across the top surface back toward the nozzle by 50 pct and creates a slight drift toward the wide faces. Both of these effects disrupt the mainly 2-D flow pattern found without gas. These predictions agree with the observations in water models reported by others.[27]

Gas bubbles are predicted to have much less effect on the flow pattern in the lower portion of the mold. The lower recirculation zone appears very similar to that without gas, with the lower eye raised only a small distance. The reason for this diminished effect is explained in Figure 5, which shows the predicted gas volume fraction for these conditions. Because of the strong buoyancy force, which is proportional to the density

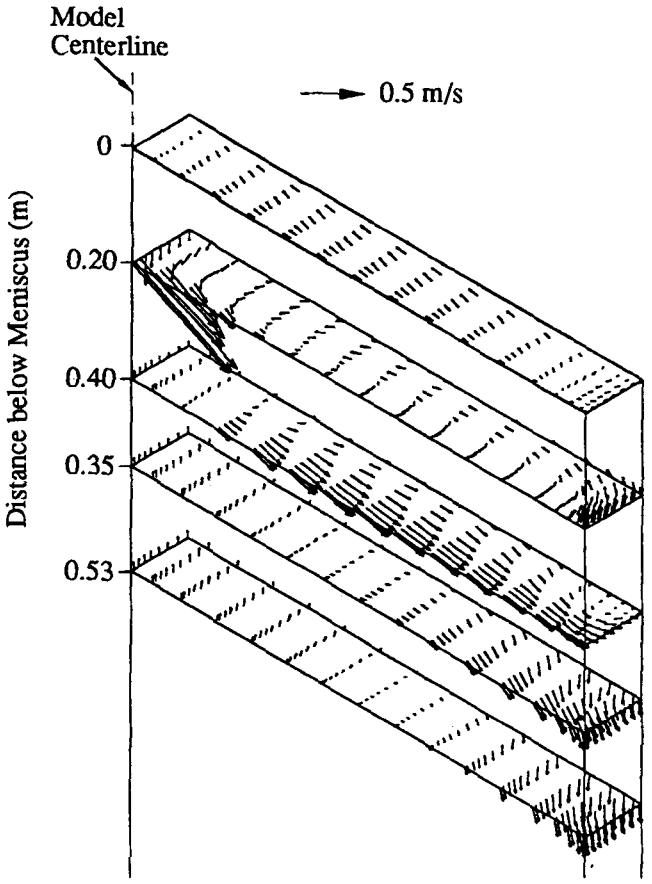

Fig. 4—Velocity vectors in transverse sections down water model (case A1 in Table I, bubble size 1 mm, 3 pct gas at inlet).

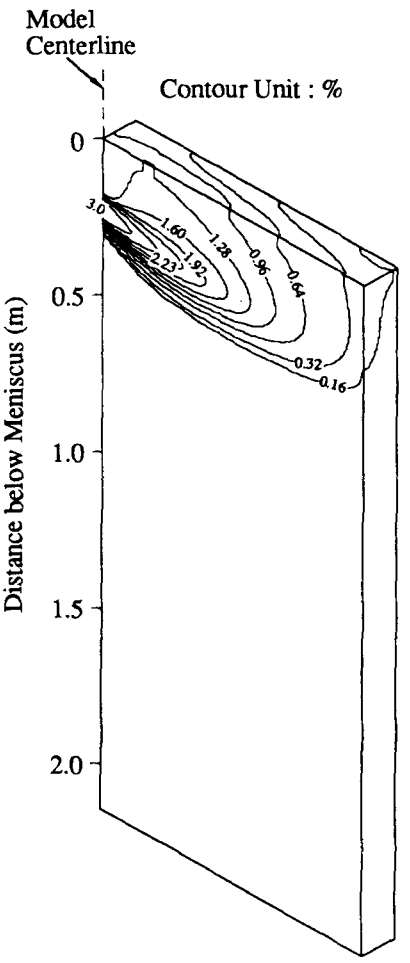

Fig. 5—Predicted gas volume fraction in water model (case A1 in Table I, bubble size 1 mm, 3 pct gas at inlet).

difference between liquid and gas, most of the gas bubbles float upward and escape from the top surface during the time that the liquid jet takes to travel from the nozzle port to the narrow face wall. Less than 5 pct of the bubbles ever reach the vicinity of the narrow wall, and even fewer enter the lower recirculation zone of the liquid flow. Thus, flow in the lower recirculation zone should be relatively unaffected by gas bubble injection.

C. *Effect of Gas Bubble Model*

The influence of the gas bubbles on the liquid has been incorporated into the model solely through the buoyancy force created by the rising bubbles. There are at least two other factors, ignored in the present model, which are worthy of further discussion. The first is the effect of the momentum imparted from the bubbles to the liquid. This is expected to be negligible because of the small bubble size combined with the very small gas density relative to the liquid. The second effect is the reduction in the volume fraction of the liquid due to the presence of the gas bubbles. A preliminary study incorporating this effect into the model revealed that correctly decreasing the liquid volume increases liquid velocities near the inlet port. Elsewhere, however, there are no significant changes in either the velocities, temperature predictions, or agreement with experiments.

VII. PHYSICAL WATER MODEL EXPERIMENTS

To verify the numerical flow model predictions, measurements of velocity profiles and flow pattern observations have been made with full-scale water models at Armco Research Center (Middletown, OH) and Inland Steel (East Chicago, IN). The 1.93-m- (76-in.-) wide and 0.229-m- (9-in.-) thick "water caster," shown schematically in Figure 6, is a clear plastic representation of an actual slab caster used in the Armco Middletown Works, with its length shortened to 2.15 m. This physical model has four pipes located at the bottom of the wide face to allow removal of water at a volume flow rate corresponding to the casting speed. Helium gas was injected into the slide gate on some trials to simulate argon injection through the submerged entry nozzle at the steel caster.

The flow patterns are visualized in three ways: (1) blue ink injected as a pulse from the tundish slide gate; (2) observation of a flag constructed with thin film attached to a wooden dowel; (3) helium gas bubbles injected through the SEN. Observations using these three methods are combined to estimate the average downward angle of the jet traversing the mold, the impingement point of the jet against the narrow face, and the

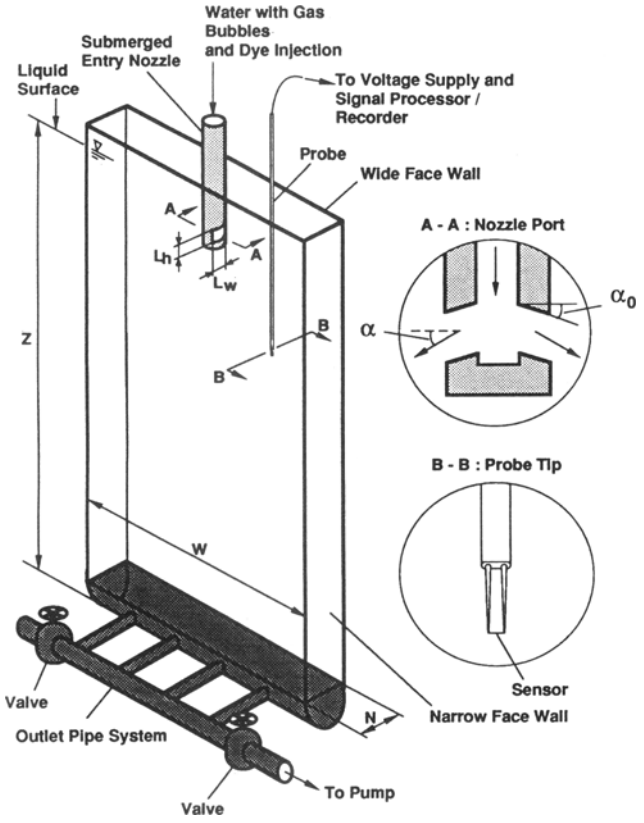

Fig. 6—Schematic of physical water model and hot-wire anemometry apparatus for speed measurements.

locations of the centers of the upper and lower recirculation zones.

A hot-wire anemometer probe with a single-wire sensor is used to measure the velocity profiles. Carefully measured resistance heating power is provided to the wire to balance the heat loss, which increases in proportion to the flow velocity component perpendicular to the wire. By orienting the sensor wire perpendicular to the wide face wall, this probe measures the speed component in the wide face plane. The calibrated voltage signals from the sensor are recorded by both a strip chart and a needle, whose movements are dampened electronically to produce a partially time-averaged signal.

After careful calibration of the system, including an adjustment for water temperature, the probe was traversed manually across the mold at the symmetry plane through the narrow face of the water model. Measurements were taken at 50-mm intervals down each vertical line from the top surface. Extra data points were measured near the nozzle port and impingement point, as determined by flow pattern visualization, because large velocity gradients were expected in these regions.

A typical signal output from the strip chart recorder is shown in Figure 7. For this example, the time-averaged speed is 0.23 m/s, and the standard deviation, containing 68 pct of the signals, is about 0.08 m/s. Note that the maximum range of the signal is ±0.18 m/s, indicating the tremendous effect of the time-dependent turbulent fluctuations of the flow field. The jet is observed

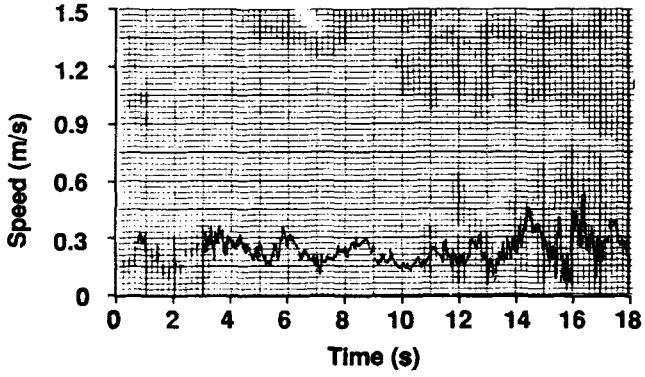

Fig. 7—Typical signals output from the strip chart record (mean velocity = 0.23 m/s; standard deviation = 0.08 m/s).

to "wander" around with time, producing a low-frequency variation in the velocity signal of 2 to 5 seconds. To account for this effect and to ensure that a true time-mean speed measurement was obtained, over 2 minutes of signal measurements were averaged to obtain each speed data point.

VIII. NUMERICAL MODEL VALIDATION

To validate the accuracy of the numerical flow model, described in Section III, simulations were run to match the flow conditions in the full-scale physical water models described in Section VII. This section compares the numerical predictions with the experimental observations of flow pattern, gas bubble distribution, and speed measurements.

A. *Comparison with Flow Pattern Observations*

The overall flow pattern calculated numerically is very similar to the flow pattern observed in the physical models. Table II quantitatively compares the flow parameters for simulation conditions, case A1 in Table I, matching experiments performed at Armco Research.[42] For the comparisons with gas, the gas volume fraction, σ_{g0}, of 3 pct (corresponding to 0.00022 m^3/s), was chosen to approximate the flow rate of 0.5 SCFM (standard cubic feet per minute) of helium injected into the physical model nozzle through a small tube of inner and outer diameter of 4 and 6.4 mm, respectively. The bubble size of 5 mm was estimated both by visual observations and by examining photographs of the bubbles in the water model.

The five measurements of eye and impingement point location agree with the numerical predictions both with and without gas. The largest discrepancy is the slightly deeper lower eye predicted by the numerical model. This might be because the jet in the physical model achieves fully developed turbulent channel flow more rapidly than in the computational model cavity. Consequently, the recirculation zone in the physical model is shortened.

The flow predictions agree with the measurements that the effect of the gas bubbles on the flow pattern is quite small, for this case with only 3 pct gas injection. As seen in Table II, gas bubbles consistently raise the depth of

Table II. Experimental and Predicted Eyes and Impingement Point in Water Model (Case A1 in Table I)

	No Gas		With Gas	
	Predicted	Experimental	Predicted (Size 5 mm, 3 pct Gas)	Experimental
Lower eye:				
Distance to centerline (m)	0.521	0.55	0.521	0.53
Depth (m)	1.143	0.80	1.041	0.76
Upper eye:				
Distance to centerline (m)	0.521	0.55	0.579	0.53
Depth (m)	0.254	0.20	0.198	0.24
Impingement point depth (m)	0.498	0.50	0.442	0.48
Jet angle (°)	25 down	28 down	25 down	29 down
Surface speed (m/s) (midway between nozzle and narrow face at centerplane)	0.23	0.25	0.11	—

the impingement point and the lower eye. Although small, the direction of movement of the upper eye does not agree. This might be due to the difficulty in measuring this location, which wanders with time and is not uniform through the thickness of the water model.

B. *Comparison with Speed Measurements*

Predicted velocity profiles are compared in Figure 8 with experimental speed measurements on the Armco water model for simulation conditions corresponding to cases A2 and A3 in Table I. This figure shows an agreement between predicted and measured velocities, both qualitatively and quantitatively. The results show how the jet spreads as it moves across the mold. Its peak velocity decays to about 30 pct of the inlet value by the time the jet is halfway to the narrow face wall. Near the narrow face wall, the velocity profile has a concave shape, due to stagnation at the point of impingement. Note in Figure 8(b) that speeds measured earlier (solid circles)[43] are larger than recent measurements (open circles), which agree more closely with the numerical predictions.

No major differences are seen between the velocities produced by the different nozzle port shapes compared in Figures 8(a) and (b). The characteristics of the rectangular and circular nozzle ports compared here are given in cases A2 and A3 in Table I. The separate 3-D model of nozzle flow found that these two nozzles produce jets with a similar angle, outlet area, and flow rate, despite differences in their nominal geometries.[29] Both the mathematical and physical models show that the two ports produce similar velocity profiles in the mold as well, except for a small difference in magnitude, which is reproduced by the calculations. This implies that the steady flow pattern in the mold is controlled solely by the angle, outlet area, and flow rate of the jet exiting the nozzle. Thus, nozzle port shape alone should have no significant effect on the flow pattern and related phenomena. This might appear to contradict other work, which has reported an important influence of nozzle port shape on turbulence at the meniscus.[44] However, the present work concludes only that the nozzle port shape alone has no effect on the time-mean flow pattern. Nozzle shape might affect the casting process through its influence on nonsteady phenomena, such as time variations in turbulence or asymmetric surging, which require further study.

Figure 9 shows the similarity between the predicted and measured effects of gas bubble injection on the speed profiles down the mold interior. As observed visually, a 3 pct injection of 1-mm-diameter helium bubbles has a relatively small effect on the jet. Predictions and measurements both show that gas injection widens the jet slightly and diminishes its peak. Quantitatively, the measurements are consistently higher than the numerical predictions, as expected from the discussion of Figure 8(b).

Reasonable agreement between predicted and measured velocities is seen again in Figure 10. The experimental data shown in this figure were obtained at Inland Steel[45] and correspond to the simulation conditions given in case B1 of Table I. The velocity stagnation at the impingement point, which traverses speed only 5 mm from the narrow face wall, is particularly evident in this figure, both experimentally and numerically. The stagnation point falls between adjacent velocity peaks, where the jet splits to flow upward and downward along the narrow face. These measurements also show that the speed on the right side of the water model is higher than the left side, due to the asymmetrical opening of the nozzle slide gate.[45] This flow asymmetry was not accounted for in the numerical model results reported here. Nevertheless, the numerical model is able to reproduce the main flow characteristics, including the locations of impingement point and velocity peaks. Speed predictions match the measurements down the left wall quite closely. Note that relatively little difference is predicted between speeds at 7 and 14 mm from the wall.

It is interesting to note a slight overprediction of the measured velocity between 1 and 2 m below the meniscus. This has been postulated to arise from the numerical model's neglect of strand curvature, which was present in the physical model. As the strand curves away from the vertical nozzle, the greatest intensity of the jet down the narrow face wall should move closer to the outer radius. This should leave lower speeds at the center

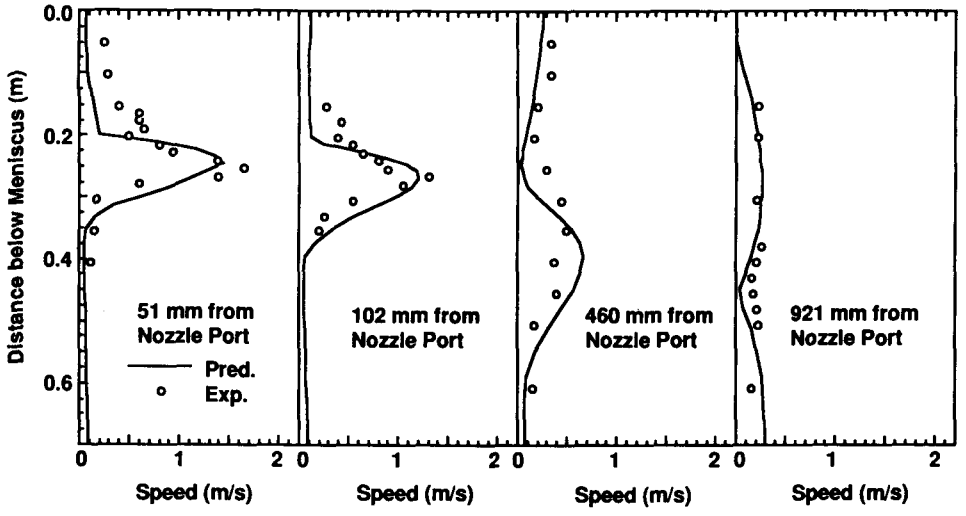

(*a*)

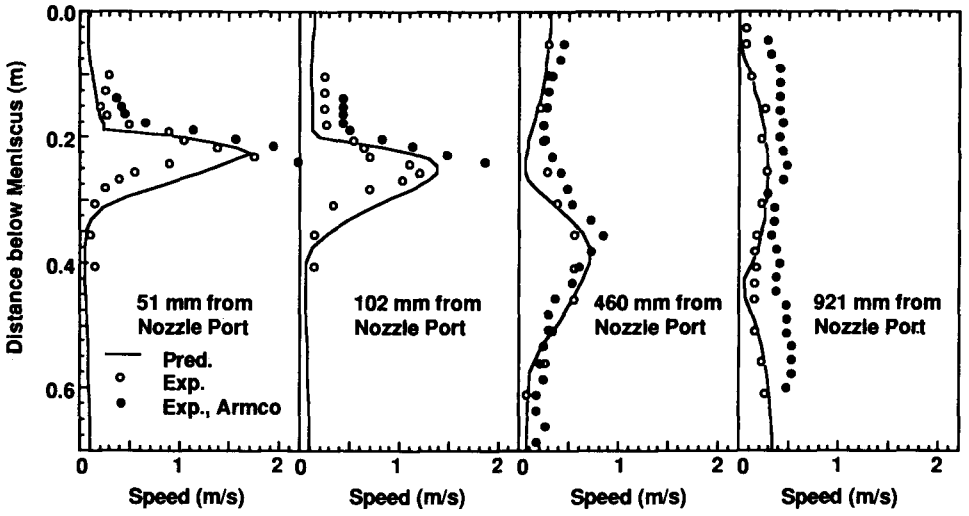

(*b*)

Fig. 8—Comparison of calculated and measured velocity profiles in water model (cases A2 and A3 in Table I). (*a*) 51-mm (1-in.) by 89-mm (3.5-in.) rectangular nozzle port (case A2 in Table I) and (*b*) circular nozzle port with a diameter 51-mm (2-in.) (case A3 in Table I).

plane, where speeds are compared in Figure 10. Strand curvature was expected to cause a difference between predicted and measured speeds, but the actual difference was surprisingly small, which indicates that the flow tends to bend to follow the strand curvature.

The greatest discrepancies between speed measurements and calculations exist in the low-velocity areas of the mold. These include the velocity valley corresponding to the upper eye in the 460-mm frames of Figure 8, and the valley near the impingement point in the 10-mm frames of Figures 8 and 10. Measured values in these regions are somewhat higher than the predictions for several reasons. First, it is very difficult to measure the flow near separation, reattachment, or impingement points, which have low time-averaged velocity but high turbulence levels. The eyes and impingement points were observed to move around with time, so their locations are difficult to specify exactly. Second, the single-sensor probe used in these experiments measures only speed (velocity magnitude) and cannot detect reversals of flow direction, such as caused by turbulence. Because speeds are always recorded as positive, larger time-averaged speeds are measured in these regions where rapid flow reversals are common. The same observation has been found for flow in nozzles.[29] Finally, there may be large-scale transient effects that cannot be detected with the steady-state calculations.

C. *Comparison with Gas Bubble Distribution Observations*

Accurate calculation of bubble distribution is important because gas bubbles affect the liquid flow pattern in proportion to the calculated gas volume fraction, σ_g, in the present model. The calculated gas volume fractions and corresponding flow pattern are compared in Figure 11 with those observed at Inland Steel[30,45] under conditions B2 of Table I. The model predicts the same tendency for gas bubble movement as shown in the photograph. Most of the bubbles are crowded together in the upper region of the mold cavity. After entering

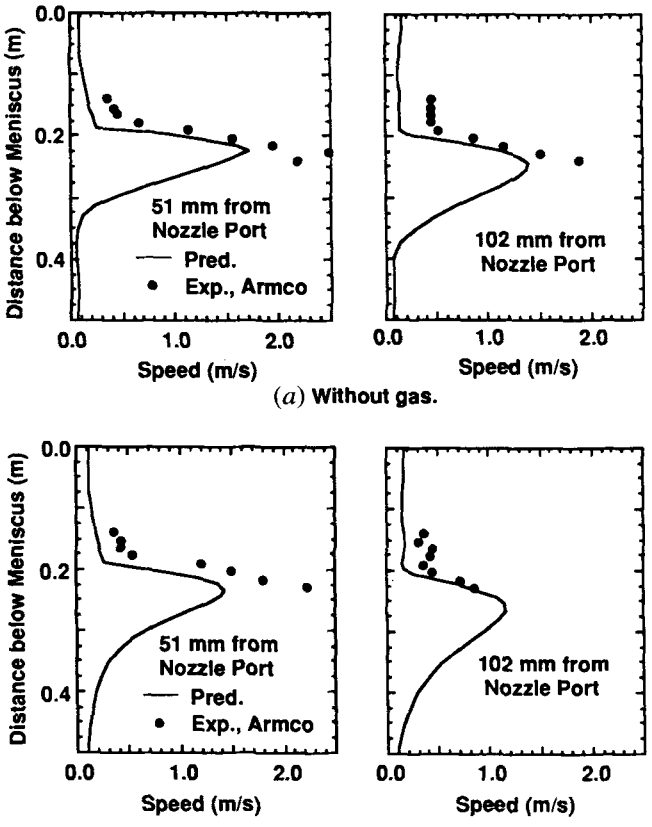

Fig. 9—Comparison of calculated and measured velocity profiles near nozzle port in water model (case A2 in Table I).

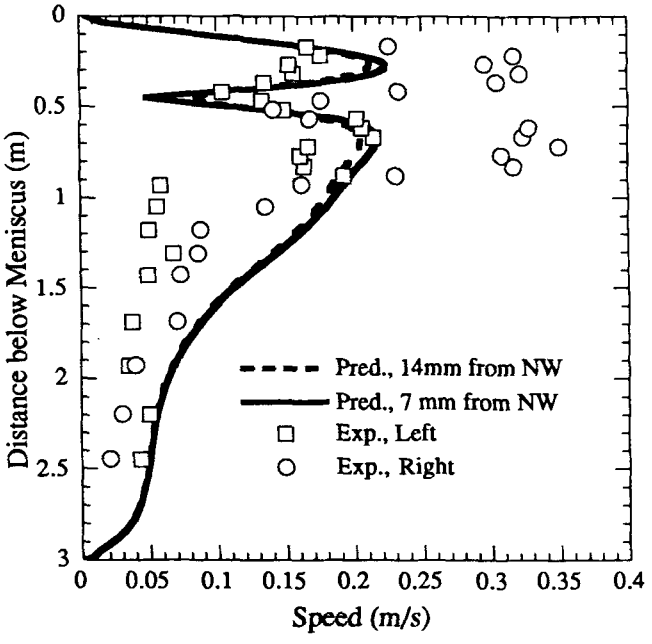

Fig. 10—Comparison of predicted and measured velocity profiles near narrow wall in water model (case B1 in Table I).

the mold cavity with the liquid jet, the bubbles float quickly upward through the recirculation zone, and leave the top surface at their assumed terminal velocity, v_{gt}, (0.12 m/s for 1-mm bubbles). Fewer and fewer bubbles stay in the jet as it travels across the mold. This figure also shows that the flow pattern predictions are reasonable, and it illustrates how the bubbles buoy the liquid jet slightly upward.

The model somewhat underpredicts bubble penetration to the deeper regions of the mold cavity. Several reasons are suspected: (1) stronger turbulence in the physical water model gives rise to higher turbulent dispersion than that predicted; (2) real, nonspherical bubbles have higher drag, so they are carried further by the liquid jet; (3) bubbles do not leave the top surface at their terminal velocity, as assumed by the model. Instead, they collect at the meniscus under the action of surface tension forces, which likely prolongs their average residence time.

D. *Verification of Heat- and Mass-Transfer Models*

The heat- and mass-transfer models developed and described in this work have been compared favorably with available data from plant trials, including measured liquid temperature,[37] shell thickness,[46] and slab composition.[42,47] Further discussion of the details of these comparisons, as well as model results and parametric studies, is given elsewhere.[33,40]

IX. EFFECT OF ARGON GAS INJECTION IN STEEL CASTER

The extensive validation with water models, presented in Section VIII, generates some confidence that the numerical models are capable of making reasonable predictions of multiphase flow, heat transfer, and mass transfer, in the mold region of actual continuous steel slab casters. The models are next applied to investigate the effects of argon gas injection on these phenomena under the typical casting conditions listed in Tables I (case C) and III.

A. *Bubble Expansion*

The gas volume fraction and bubble size at the inlet (corresponding to the nozzle port) were determined by considering the significant volume expansion that should occur as the bubbles heat up while traveling down the nozzle. This effect magnifies the importance of argon gas in a steel caster, compared to that in a water model. The bubble expansion and the corresponding increase of gas volume flow rate into the mold are calculated according to the equations in Section II and data in case C of Table I. The temperature rise almost doubles the bubble diameter, which increases the gas volume flow rate at the nozzle outlet to about five times higher than that injected into the nozzle at standard conditions (25 °C and 1 atm). Setting the gas volume flow rate into the nozzle inlet at standard conditions to be 0.00026 m^3/s (0.55 SCFM or 5 pct) and expanding 3-mm bubbles by a factor of 5.2 produce a 22 pct volume fraction of 5-mm bubbles at the inlet to the mold (case C of Table I). The

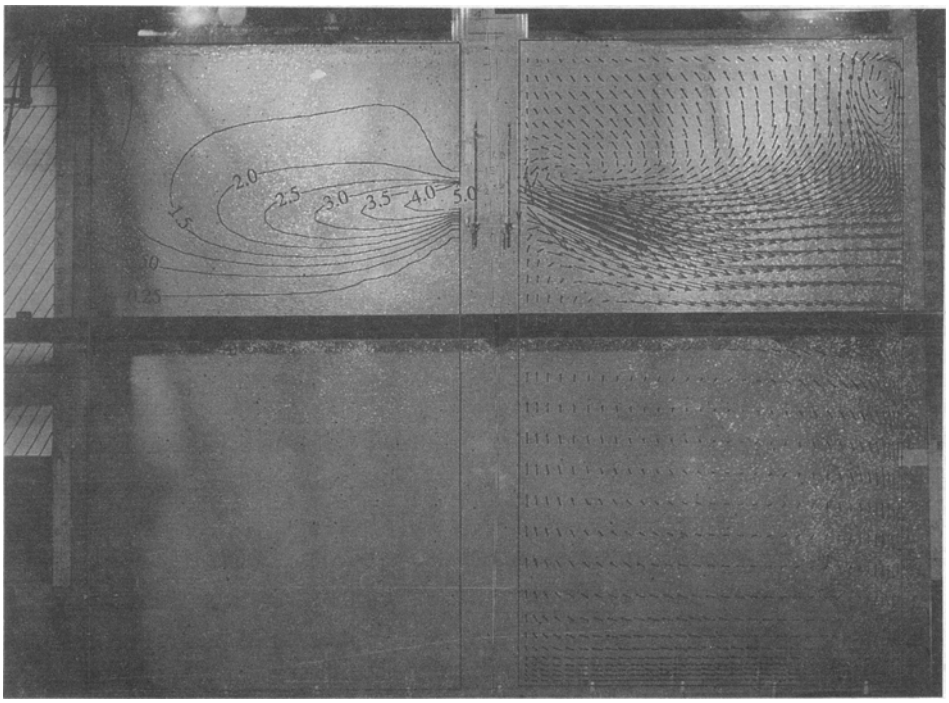

(a) Gas volume fraction (contour unit : %)

(b) Liquid velocities (→ 0.3 m/s)

Fig. 11—Comparison of calculated and measured velocities and gas volume fraction in water model (case B2 in Table I).

Table III. Simulation Conditions for Heat-Transfer Model**

C_p	680 J kg^{-1} K^{-1}
h	40 W m^{-2} K^{-1}
k_0	26 W m^{-1} K^{-1}
Pr_0	0.1
Pr_t	0.9
T_{liq}	1525 °C
T_0	1550 °C
T_{sol}	1518 °C
T_∞	27 °C
ΔT_s	25 °C

**Unlisted values are the same as case C of Table I.

volume increase due to heating is over 10 times more important than the volume change due to the pressure change. Moreover, calculations in the Appendix show that this heating is extremely rapid and is completed well before the bubbles enter the mold cavity. Thus, it is reasonable to ignore the effects of temperature and pressure changes on bubble behavior in the mold cavity itself. The argon flow rates of 0 to 22 pct with sizes of 1 to 5 mm at the mold inlet were chosen in this study to represent the typical range of gas injection practices encountered in different casting operations.

B. *Flow Pattern*

Argon gas injection affects the casting process in part through its influence on the liquid flow pattern. The extent of this effect depends on both the gas injection rate and the bubble size. Figures 12 and 13 show the effects of these two important parameters on the liquid flow patterns and the movement of gas bubbles themselves, for typical casting conditions. In contrast to flow in the water model, 0.00026 m^3/s gas injection into a steel caster produces a substantial change in the flow pattern, as the gas fraction entering the mold increases from 5 to 22 pct as a result of the gas expansion discussed in Section A. When argon is present, the upper recirculation zone shrinks to a very small region near the nozzle and may even disappear altogether. Flow across the surface of the mold completely reverses, as increased flow toward the surface takes liquid back toward the narrow face. The lower recirculation eye and impingement point shift upward markedly. Figure 13 shows that most bubbles are concentrated in the central portion of the wide face. More than 25 pct of the bubbles are predicted to impinge upon the upper portion of the wide face walls, during their upward flotation.

1. *Effect of gas injection rate*

Figure 12 shows that increasing the gas volume flow rate entering the mold produces a corresponding increase in its effect. Stronger buoyancy due to the introduction of more bubbles not only changes the flow pattern to a larger extent, but also makes the bubbles themselves float more easily, resulting in shallower bubble dispersion in the mold. Figure 13 shows that bubble concentration in the mold naturally increases with increasing volume fraction at the inlet. However, the effect is not directly proportional.

2. *Effect of gas bubble size*

Argon bubble size has an important effect that is independent of injection rate. Larger bubbles are predicted

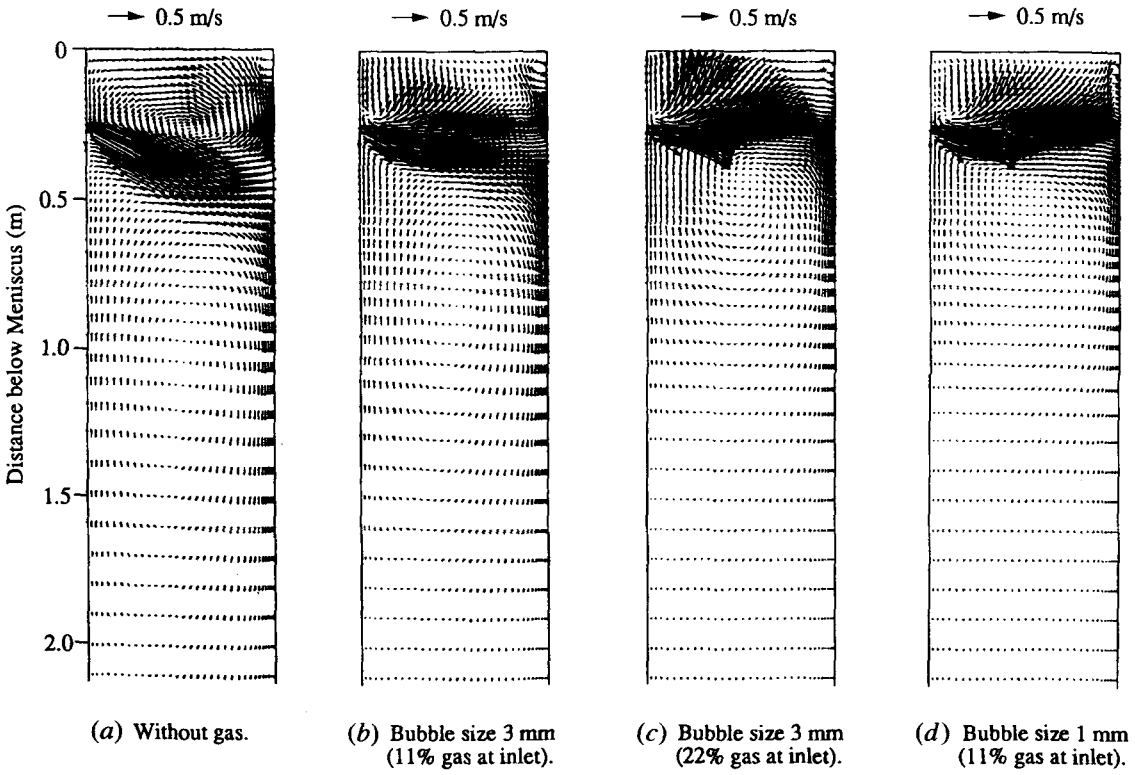

Fig. 12—Effect of argon gas bubble size and injection rate on flow pattern in steel caster.

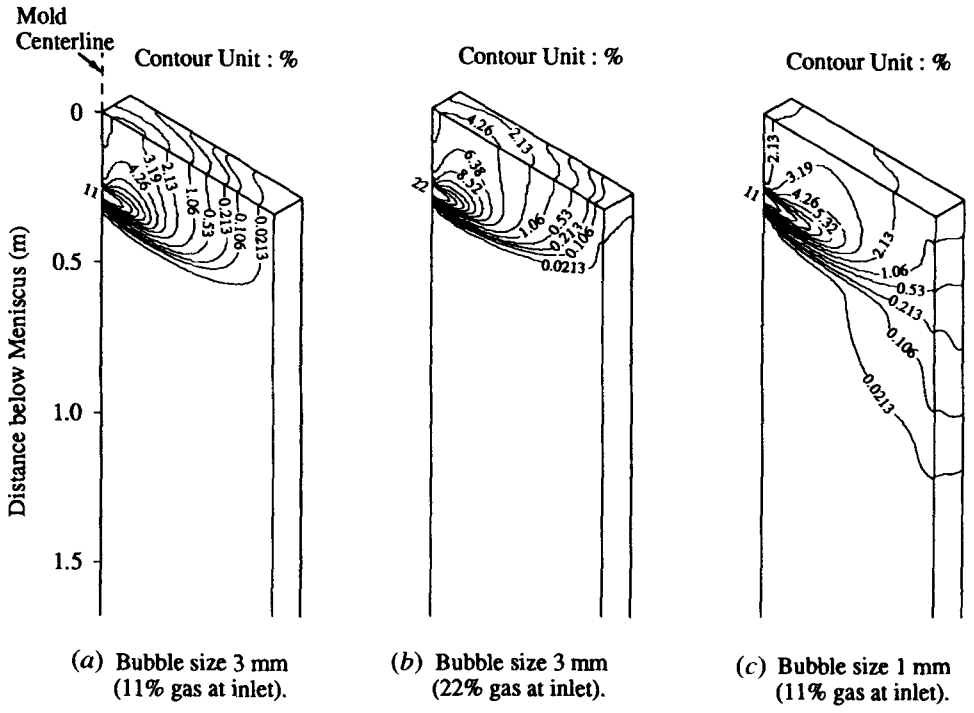

Fig. 13—Effect of argon gas bubble size and injection rate on distribution of gas volume fraction in steel caster.

to leave the mold faster and, therefore, to have less influence on the liquid flow pattern. A comparison of Figures 12(b) and (d), or Figures 13(a) and (c), shows that smaller bubbles penetrate further across the mold. The concentration contours show that about 1 in every 10 1-mm bubbles reaches the narrow face, compared with less than 1 in 100 for 3-mm bubbles. This accounts for the greater influence of small bubbles on the flow pattern. Some of the small bubbles may penetrate into the lower recirculation zone, particularly in narrow molds. Entrapment deep in the caster is unlikely to present a serious quality problem, however, as it should be

extremely rare for large bubbles. The distribution of small bubbles leaving the top surface is relatively uniform, while large bubbles are concentrated near the nozzle.

C. *Heat Transfer*

The effect of argon injection on temperature and superheat dissipation is shown in Figures 14 through 18 and Table IV. Compared with the flat temperature distribution across the mold width when there is no gas (Figure 14(a)), argon bubbles buoy hotter steel to the top surface, changing its temperature from coldest (1527 °C) at narrow face wall to highest (1531 °C) halfway across the mold, then to medium (1529 °C) close to the nozzle wall (Figure 14(b)). Although argon raises the surface temperature only a few degrees, this small temperature difference may be very important to solidification at the meniscus.

Figures 15 through 18 and Table IV show the effect of argon injection on the "superheat flux" transported across the interface between the liquid steel and the solidifying shell against the narrow and wide faces. The argon gas produces a significant increase in superheat flux to the upper portion of the wide face, and the meniscus region in particular, where superheat flux is almost doubled. The upward shift in flow causes a greater portion of the superheat to be removed in the mold and

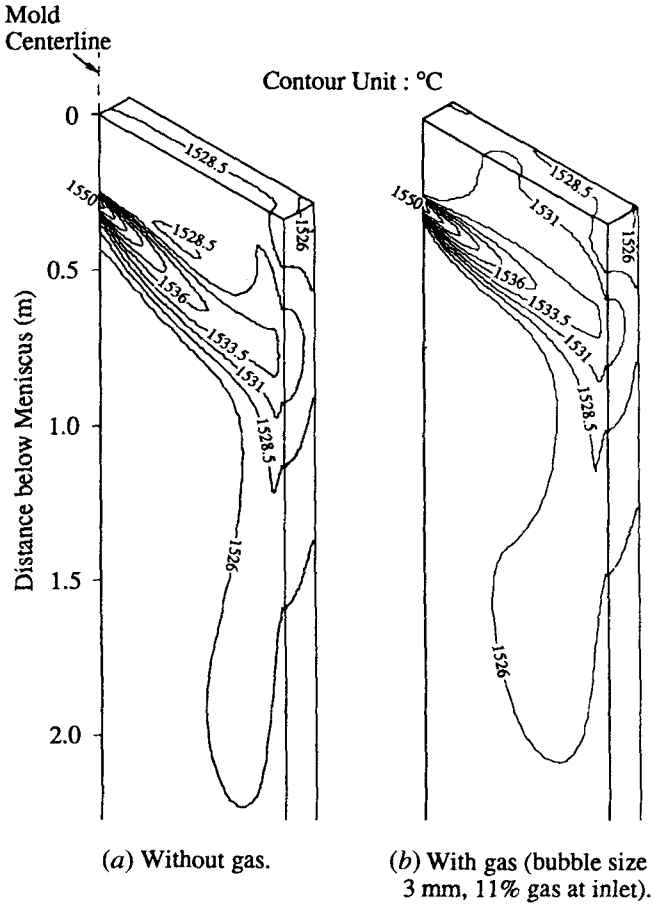

(*a*) Without gas. (*b*) With gas (bubble size 3 mm, 11% gas at inlet).

Fig. 14—Effect of argon gas bubbles on temperature distribution in steel caster.

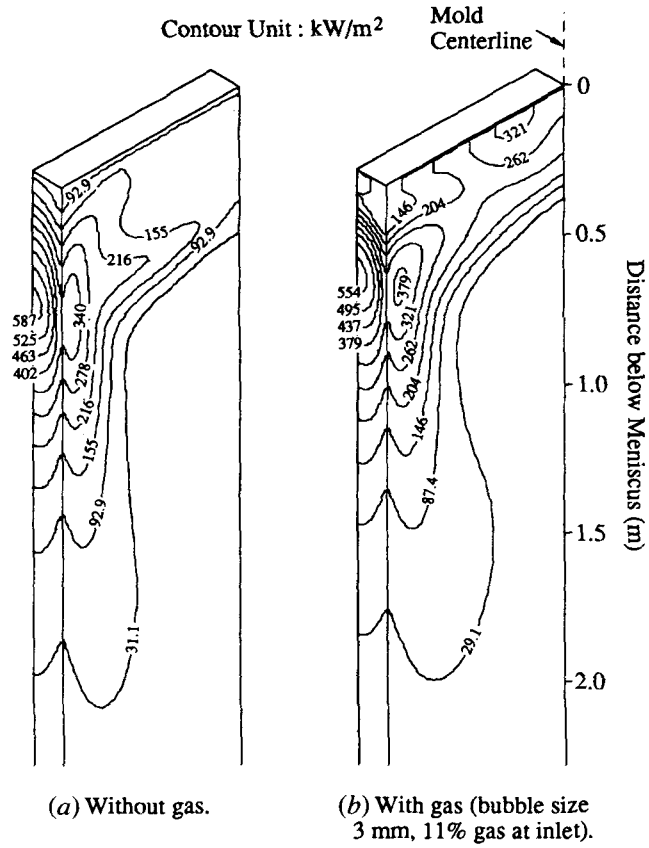

(*a*) Without gas. (*b*) With gas (bubble size 3 mm, 11% gas at inlet).

Fig. 15—Effect of argon gas bubbles on heat flux distribution in steel caster.

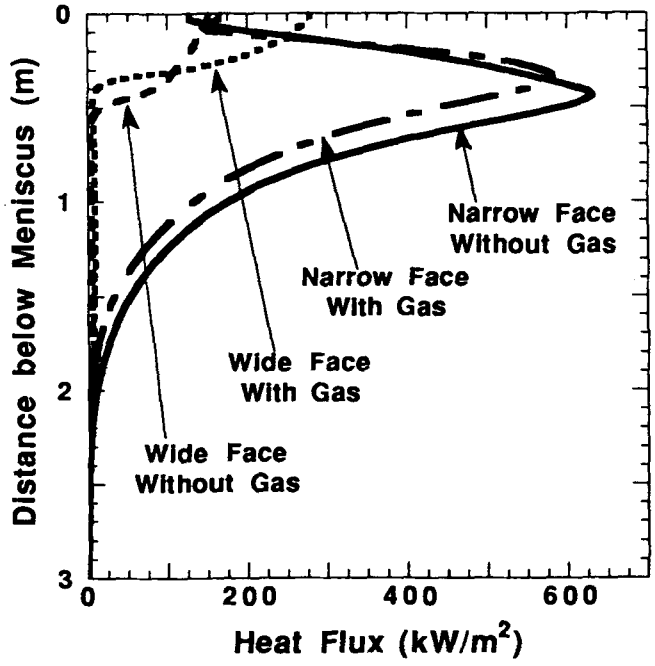

Fig. 16—Effect of argon gas bubbles on heat flux along centerlines of wide and narrow faces (bubble size 3 mm, 11 pct gas at inlet).

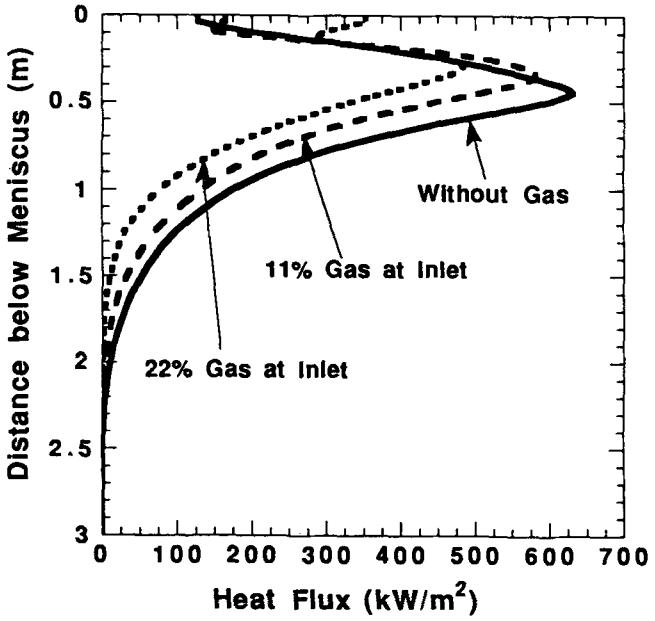

Fig. 17—Effect of argon gas injection rate on heat flux along narrow face centerline (bubble size 3 mm).

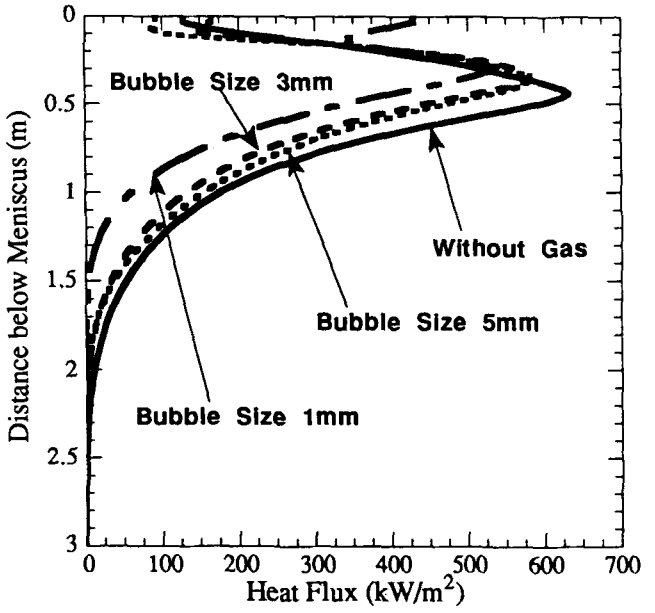

Fig. 18—Effect of argon gas bubble size on heat flux along narrow face centerline (11 pct gas at inlet).

moves the hottest impingement point further above the mold exit. The peak superheat flux associated with the narrow face impingement point is very slightly smaller than that without gas. These side effects of argon use could be beneficial in decreasing the potential dangers related to inadequate liquid superheat at the meniscus and possibly also thinning of the narrow face shell.

1. *Effect of gas injection rate*

Increasing argon injection rate amplifies its effect on heat transfer, in accordance with its effect on the flow pattern. This is shown in Figure 17 and Table IV. Increasing injection causes a greater upward shift of the impingement point and a bigger drop of the superheat flux peak value. It should be noticed that more than 80 pct of the total superheat is transferred to the wide face for the case with 22 pct 3-mm bubbles (Table IV). This compares to 70 pct without gas.

2. *Effect of gas bubble size*

The effect of gas bubble size can be seen in Figure 18 and Table IV. The smaller the bubbles, the stronger their effect. The narrow face impingement point shifts upward, and the peak value of heat flux decreases systematically with decreasing bubble size (Figure 18). The total superheat transferred to the shell inside the casting mold increases from 60 pct (without gas or with 5-mm bubbles), to 65 pct (with 3-mm bubbles), to 74 pct (with 1-mm bubbles). Heat delivered to the meniscus is also much greater for the smaller bubbles.

D. *Mass Transfer*

The effect of argon gas bubbles on slab composition during a steel grade transition was investigated by running the 3-D mass-transfer model, described in Section V, under the conditions listed as case C in Table I (both without gas and with 11 pct 3-mm bubbles). A solidification constant, k_{shell}, of 0.00327 $m/s^{0.5}$ was assumed for the parabolic shell growth function, which generates a liquid pool length (metallurgical length) of 19.6 m.

The resulting composition profiles down the solid slabs are shown in Figure 19. Surface composition changes slightly when argon is introduced into the casting mold. Argon injection transports new grade to the meniscus faster, thereby slightly reducing the extent of intermixing along the slab surface.

There is no measurable change in mixing along the centerline of the slab, however. The effect of argon gas on slab composition is smaller than that on superheat removal because bubbles only affect the very top portion of the strand (upper 0.5 m). The slab composition depends on mass transfer in the entire liquid pool, which is more than an order of magnitude longer. The effect of argon decays very rapidly with distance from the meniscus, and almost completely disappears below about 3 m down the strand, where the solidified shell is only about 45-mm thick. Thus, internal mixing behavior below this depth is expected to be unchanged, as observed in Figure 19. Intermixing of grades extends to a significant distance down the slab centerline and is governed by turbulent diffusion, as discussed and verified in previous work.[40]

X. IMPLICATIONS FOR STEEL QUALITY

Flow in the liquid cavity of a continuous steel caster is greatly affected by argon gas injection. This has important consequences for steel surface quality, through its effect on surface turbulence, entrapment of bubbles and inclusions, and superheat delivered to the meniscus region. This section explores the implications of the model results on these quality issues.

A. *Surface Turbulence*

The momentum of fast-floating large (>3 mm) bubbles is likely to generate tremendous surface turbulence

Table IV. Predicted Superheat Distribution

Superheat Lost to:	Without Gas Heat Flow (kW)	Without Gas Pct	Size 5 mm, 11 Pct Gas Heat Flow (kW)	Size 5 mm, 11 Pct Gas Pct	Size 3 mm, 11 Pct Gas Heat Flow (kW)	Size 3 mm, 11 Pct Gas Pct	Size 1 mm, 11 Pct Gas Heat Flow (kW)	Size 1 mm, 11 Pct Gas Pct	Size 3 mm, 22 Pct Gas Heat Flow (kW)	Size 3 mm, 22 Pct Gas Pct
Conduction through top surface flux layer	11.3	1.9	11.3	1.9	11.3	1.9	11.3	1.9	11.3	1.9
Convection to shell inside mold (0 to 0.6 m)										
Narrow face	99.7	17.1	92.3	15.9	91.6	15.7	91.6	15.7	82.1	14.1
Wide face	255.1	43.8	256.2	44.0	290.3	49.9	340.7	58.5	307.6	52.9
Convection to shell just below mold (0.6 to 1.6 m)										
Narrow face	67.5	11.6	56.0	9.6	49.2	8.5	25.6	4.4	30.7	5.3
Wide face	118.2	20.3	147.3	25.3	123.2	21.2	117.7	20.2	150.5	25.9
Convection to shell farther below mold (1.6 to 3.0 m)										
Narrow face	4.8	0.8	2.2	0.4	2.4	0.4	0.3	0.1	0.7	0.1
Wide face	37.3	6.4	31.2	5.4	28.3	4.9	7.3	1.3	12.1	2.1
Dissipation very low in caster (below 3.0 m)	0.9	0.2	0.5	0.1	0.5	0.1	0.0	0.0	0.1	0.0
Total	594.8	102.2	597.0	102.6	596.8	102.5	594.5	102.1	595.1	102.3
Superheat into mold	582.0		582.0		582.0		582.0		582.0	
Numerical convergence errors	12.8	2.2	15.0	2.6	14.8	2.5	12.5	2.1	13.1	2.3

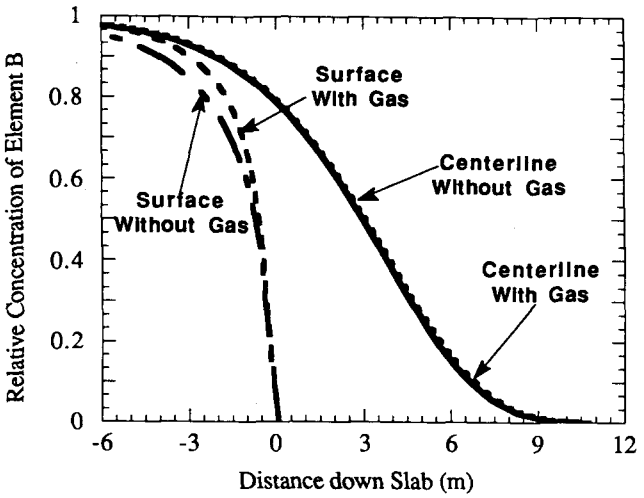

Fig. 19—Effect of argon bubbles on composition along slab casting direction during a steel grade transition (bubble size 3 mm, 11 pct gas at inlet).

when the bubbles explode through the top surface, thereby presenting a great quality hazard. The predicted argon distributions (Figure 13) suggest that surface quality problems due to this should be greatest near the central portions of the wide face, where most of the large bubbles escape. Nonuniform oscillation marks and defects, such as trapped mold slag, which are concentrated on the central surface of the wide face of the strand could be evidence of surface turbulence, level fluctuations, and interrupted liquid powder feeding generated by excessive argon.

To minimize this quality problem, excessive numbers of large argon bubbles should be avoided. Bubble size is difficult to control because turbulent fluid flow may affect the shear forces inside the nozzle walls that govern the initial bubble size, and may break up or combine bubbles after their formation. The more practical solution is simply to reduce the argon injection rate to the minimum possible. Slide gate flow control systems appear to be inherently prone to more quality problems related to excessive gas injection than stopper rod systems, because of their dependence on argon injection to prevent air aspiration between the plates.

In addition to the increased disturbance of the surface caused by escaping bubbles, argon injection also affects surface turbulence through its major influence on the average flow pattern. Quality problems due to surface turbulence have been found to correlate with the speed of the fluid flowing across the top surface.[48] Lower average surface speeds create fewer level fluctuations and are less likely to entrain liquid flux.

Increasing argon injection has been shown to direct increasing flow toward the top surface. High argon levels ($\sigma_{g0} > 11$ pct) create strong flow across the surface toward the narrow face (Figure 12), so they are detrimental for a second reason. However, small amounts of argon injection (such as $Q_g = 0.00005$ m^3/s or $\sigma_{g0} = 5$ pct for the casting conditions assumed here) tend to cancel the general recirculating flow of liquid from the narrow face back toward the nozzle. The corresponding decrease in average surface speed may be beneficial.[27]

An optimum argon injection rate may exist for a given casting operation. This rate depends on the other factors that control the flow pattern, such as nozzle geometry and submergence depth. It also must change with casting speed, in order to maintain the optimum gas volume

fraction. Excessive gas turbulence will occur during slowdown periods if the argon injection rate is not decreased proportionally. The use of argon may be an important additional parameter to control the flow pattern in the mold, particularly when casting very wide slabs.[27]

B. *Bubble Entrapment*

Pinholes and associated defects such as inclusion clusters form when bubbles that are large enough to cause a problem (>0.1 mm) are trapped near the meniscus. Smaller bubbles are more easily entrapped because they penetrate further into the strand (toward the more stagnant regions), take longer to float, and are more easily caught between dendrites in the solidifying shell. Results in Figure 13 show that the greatest meniscus concentration of the critical 1-mm bubbles occurs about midway between the nozzle and the narrow face. This suggests a slight propensity for this type of defect on this region of the slab surface.

C. *Meniscus Heat Flow*

Insufficient heat flow to the meniscus region may be responsible for quality problems related to deep oscillation marks, nonuniform flow of liquid flux, and subsurface hooks or "extended meniscus" formation. The latter has been reported to exacerbate the entrapment of solid inclusions and gas bubbles, as they float upward near to the solidification front.[48] Argon produces important changes in the dissipation of superheat by bringing hotter steel to the meniscus region. Small bubbles in particular shift superheat removal higher up the mold and greatly increase heat flow to the meniscus region. This should be beneficial for steel quality, in direct proportion to the rate of argon injection.

D. *Implications*

The results of this work indicate that argon flow rate should be adjusted according to nozzle geometry and casting conditions to achieve an optimum balance between bringing hot flow to the surface and avoiding excessive surface turbulence. Considering the other benefits of argon injection regarding the prevention of nozzle clogging, enhanced flotation of inclusions, and slightly sharper grade transitions at the slab surface, argon can be a valuable asset, if used carefully.

This work has demonstrated that mathematical models are able to quantify the steady flow pattern found in the mold cavity, and associated phenomena including the removal of superheat and the effects of argon. In addition, the behavior of large and small gas bubbles has been isolated. Surface quality depends greatly on factors such as surface turbulence, transient flow, inclusion entrapment, mold oscillation, and liquid mold flux behavior, which are not simulated directly with the present model. Thus, physical water models and controlled trials on operating steel casters remain important supplements to understanding flow phenomena. It is important to note that water model studies can and should account for the important effects of gas thermal expansion by increasing the gas injection rate about fivefold (according to Eq. [20]) to match the bubble fraction entering the mold cavity of the steel caster.

XI. CONCLUSIONS

1. Mathematical models have been developed to predict multiphase flow in the continuous slab casting process and its associated heat and mass transfer. The models are being applied to understand complex flow-related phenomena in the process.
2. Good agreement has been obtained between the flow model predictions and observations of flow pattern characteristics and speed measurements. Thus, the standard K-ε turbulence model appears able to reasonably reproduce steady-state flow in a continuous casting mold, even when there is gas injection. Other parts of the model have been validated through comparison with other experimental data.
3. Both experimental and predicted results show that there is little difference between the time-averaged flow patterns from rectangular and round nozzle ports with similar jet outlet area, jet angle, and casting conditions.
4. Argon gas bubble injection changes the flow pattern in the upper portion of the mold, shifting the impingement point and recirculation centers upward. Injection rates of 3 to 5 pct at mold inlet reduce surface speeds, while rates exceeding 10 pct can reverse the direction of flow toward the narrow face in the upper region of the mold.
5. The effects of argon gas in a steel caster are intensified, relative to water models, because of the five times gas volume expansion at high temperature and the corresponding increase of gas flow rate into the mold.
6. Increasing gas injection rate or decreasing bubble size both intensify the changes in the flow pattern.
7. Larger bubbles float more easily and leave the mold more quickly, so they have less effect on the flow pattern, but possibly more effect on surface turbulence.
8. Smaller bubbles penetrate deeper into the liquid pool, increasing their likelihood of entrapment into the solidifying shell, causing pinholes and related inclusion defects.
9. Argon gas injection causes superheat to be removed higher in the caster, moves the hot spot upward, lowers the peak superheat flux, and delivers more heat to the wide face. Both temperature and superheat flux are raised significantly in the meniscus region.
10. During a steel grade transition, argon injection only slightly affects slab surface composition and has no effect on intermixing in the slab interior.

APPENDIX

Gas expansion in casters

Bubble expansion occurs in a steel caster due to the high temperature of liquid steel. In this work, two simple models for the expansion of a single bubble heated by

high-temperature ambient fluid were developed, based on pure conduction and lumped heating with variable bubble size. These models were applied to estimate the time needed for expansion of the argon bubbles after they have been injected into the nozzle.

A. *Conduction Model*

Assuming that the ambient fluid maintains a constant bubble surface temperature T_∞, and ignoring convection and radiation inside the bubble, the governing equation and boundary and initial conditions for 1-D transient heat conduction are as follows:

$$\rho_g C_{pg} \frac{\partial T}{\partial t} = \frac{1}{r^2} \frac{\partial}{\partial r} \left(r^2 k_g \frac{\partial T}{\partial r} \right) \quad [A1]$$

$$t = 0: T = T_i \quad [A2]$$

$$t = \infty: T = T_\infty \quad [A3]$$

$$r = 0: \frac{\partial T}{\partial r} = 0 \quad [A4]$$

$$r = r_0: T = T_\infty \quad [A5]$$

$$\frac{r_0}{r_i} = \left(\frac{\rho_{gi}}{\rho_g} \right)^{1/3} = \left(\frac{T + 273}{T_i + 273} \right)^{1/3} \quad [A6]$$

where ρ_g = gas density at time t (kg m^{-3});
C_{pg} = gas specific heat = 552 (W kg^{-1} K^{-1});
k_g = gas conductivity at time t (W m^{-1} K^{-1});
T_i = initial bubble temperature = 27 (°C);
T_∞ = ambient fluid temperature = 1550 (°C);
r_0 = bubble radius at time t (m);
r_i = initial bubble size (m);
ρ_{gi} = initial gas density = 1.6 (kg m^{-3}).

Equations [A1] through [A6] are solved by a finite-difference model described elsewhere,[40] and k_g is a specified function of temperature.[49,50]

B. *Lumped Heating Model*

The lumped heating model assumes that heat transfer inside the bubble is sufficient to keep a uniform temperature inside the bubble and that the thermal resistance comes from convection with the ambient fluid. This model can be written as

$$\rho_g C_{pg} \frac{dT}{dt} = \frac{3}{r_0} h_b (T - T_\infty) \quad [A7]$$

$$\frac{r_0}{r_i} = \left(\frac{\rho_{gi}}{\rho_g} \right)^{1/3} = \left(\frac{T + 273}{T_i + 273} \right)^{1/3} \quad [A8]$$

These equations are solved for T and r_0 using the fourth-order Runge–Kutta method. The heat transfer coefficient, h_b, for this model was taken to be 100 W/(m^{2}K) from work by Iguchi and co-workers, who fitted h_b to experimental data with 30- to 40-mm bubbles.[51]

C. *Results*

The predicted change of bubble size and center temperature are shown in Figure A1 for an initial bubble size, r_i, of 10 mm, initial temperature, T_i, of 27 °C, and ambient fluid temperature, T_∞, 1550 °C. It can be seen from Figures A1 and A2 that the bubbles are heated very fast in the ambient fluid. The "heating times" (the time needed for the bubble to reach 95 pct of its final size and final temperature) obtained by the conduction and lumped heating models are 0.15 and 0.02 seconds respectively. This means that bubble heating and expansion are extremely rapid, relative to the mean residence time of bubbles in the SEN of about 0.5 second for typical casting conditions (case C in Table I with SEN

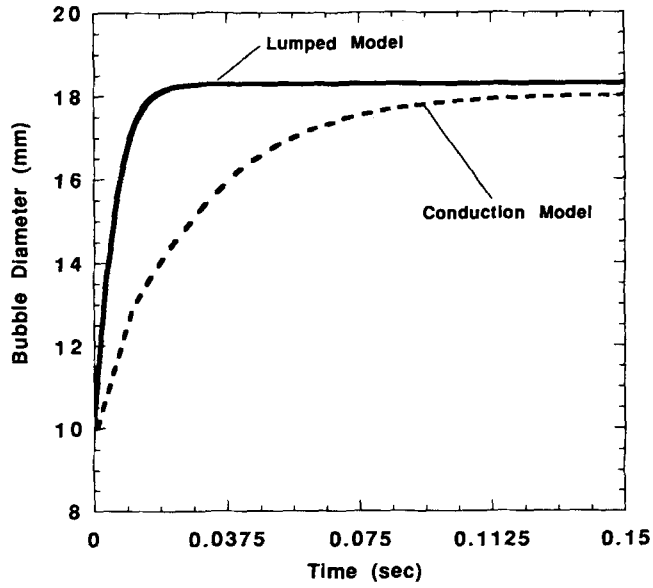

Fig. A1—Size change of a single bubble with time when heated in ambient fluid.

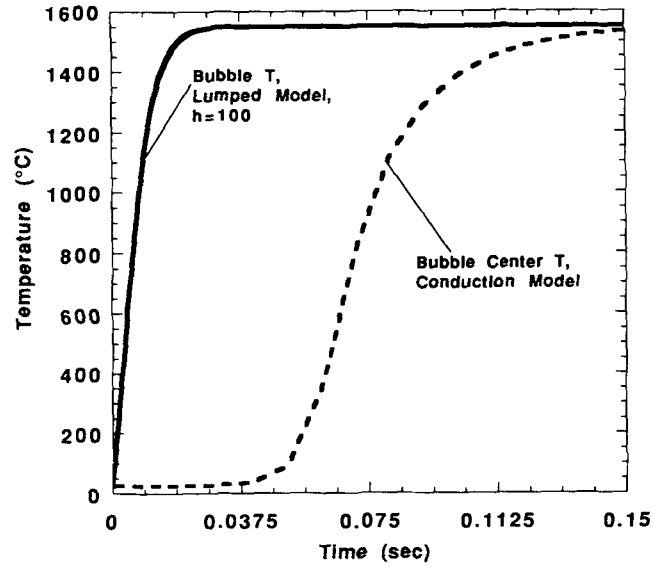

Fig. A2—Bubble temperature change with time when heated in ambient fluid.

length 0.5 m and SEN inner diameter 76 mm[52]). The lumped model is probably most accurate because the conduction model neglects the significant amount of convection inside the bubble and therefore underestimates heating rate. Even the conservative calculation demonstrates conclusively that bubble heating and expansion are finished inside the SEN. Thus, bubble size and volume fraction can be calculated by setting bubble temperature to the liquid steel temperature, as done in Section III–C of this article.

NOMENCLATURE

C	relative concentration in strand
C_p	specific heat (liquid steel) (J kg^{-1} K^{-1})
D_{eff}	effective diffusivity (liquid) (m^2 s^{-1})
D_0	molecular diffusivity (liquid) (m^2 s^{-1})
D_g	apparent gas bubble diffusivity (m^2 s^{-1})
d_g	diameter of gas bubbles entering mold (mm)
d_{gi}	diameter of gas bubbles at injection point in nozzle (mm)
E	wall roughness constant (in K-ε wall laws)
F	mass fraction of a given element
h	heat transfer coefficient (top surface) (W m^{-2} K^{-1})
K	turbulent kinetic energy (m^2 s^{-2})
K_0	turbulent kinetic energy (at inlet to mold) (m^2 s^{-2})
k_0	laminar thermal conductivity (W m^{-1} K^{-1})
K_{shell}	solidification constant (m s$^{-0.5}$)
L_0	nominal nozzle submergence depth (from top surface to top of nozzle port) (m)
L_h	inlet height (mm)
L_w	inlet width (mm)
L_n	jet submergence depth (from top surface to top of the jet) (m)
N	strand thickness (across narrow face) (m)
n	normal direction of boundaries
p	static pressure (relative to outlet plane of domain) (N s^{-2})
Pr_0	laminar Prandtl Number, $(C_p\mu_0 k_0^{-1})$
Pr_t	turbulent Prandtl Number
Q_g	gas injection rate (entering nozzle gate) (m^3 s^{-1})
Re	Reynolds number $(V_c\sqrt{NW}\rho\mu_0^{-1})$
q_{sh}	superheat flux from liquid steel to solidifying shell (W m^{-2})
Sc_t	turbulent Schmidt number $(\mu_t\rho^{-1}D_g^{-1})$
T	temperature (°C)
T_0	casting temperature (pour temperature) (at inlet to mold) (°C)
T_{liq}	liquidus temperature (°C)
T_{sol}	solidus temperature (°C)
T_∞	ambient temperature (°C)
V_c	casting speed (m s^{-1})
v_{gt}	gas bubble terminal velocity (m s^{-1})
v_{gx}	gas velocity component in x direction (m s^{-1})
v_{gy}	gas velocity component in y direction (m s^{-1})
v_{gz}	gas velocity component in z direction (m s^{-1})
v_x	liquid velocity component in x direction (m s^{-1})
v_{x0}	liquid normal velocity through inlet to mold (m s^{-1})
v_y	liquid velocity component in y direction (m s^{-1})
v_{y0}	liquid horizontal velocity through inlet to mold (m s^{-1})
v_z	liquid velocity component in z direction (m s^{-1})
v_{z0}	liquid downward velocity through inlet to mold (m s^{-1})
W	strand width (across wide face) (m)
Z	strand length simulated (m)
z	distance down strand or slab (m)
α	jet angle at inlet (Figure 6) (°)
α_0	nominal angle of nozzle port edges at inlet (Figure 6) (°)
ΔT_s	superheat temperature $(T_0 - T_{\text{liq}})$ (°C)
ε	dissipation rate (m^2 s^{-3})
ε_0	inlet dissipation rate (m^2 s^{-3})
μ_{eff}	liquid effective viscosity (kg m^{-1} s^{-1})
μ_0	liquid laminar (molecular) viscosity (kg m^{-1} s^{-1})
μ_t	liquid turbulent viscosity (kg m^{-1} s^{-1})
ρ	liquid density (kg m^{-3})
σ_g	gas volume fraction (pct)
σ_{g0}	gas volume fraction (at inlet to mold) (pct)

ACKNOWLEDGMENTS

The authors wish to thank T. Tucker and J. Hester of Armco Inc. and Y.H. Wang of Inland Steel Corporation (East Chicago, IN) for their assistance in obtaining measurements on their company water models and for providing data. The steel companies, Armco Inc., Inland Steel Corporation, LTV Steel (Cleveland, OH), and BHP Co. Ltd. (Wallsend, Australia), and the National Science Foundation (Grant No. MSS-8957195) are gratefully acknowledged for funding which made this research possible. Finally, thanks are due to Fluid Dynamics Inc. (Evanston, IL) for use of FIPOST and to the National Center for Supercomputing Applications at the University of Illinois for time on the CRAY supercomputers.

REFERENCES

1. M. Salcudean and K.Y.M. Lai: *Numer. Heat Transfer*, 1988, vol. 14, pp. 97-111.
2. M. Salcudean, K.Y.M. Lai, and R.I.L. Guthrie: *Can. J. Chem. Eng.*, 1984, vol. 63, pp. 51-61.
3. M. Salcudean, C.H. Low, A. Hurda, and R.I.L. Guthrie: *Chem. Eng. Commun.*, 1983, vol. 21, pp. 89-103.
4. D. Mazumdar and R.I.L. Guthrie: *Metall. Trans. B*, 1985, vol. 16B, pp. 83-90.
5. T.D. Roy, A.K. Majumdar, and D.B. Spalding: *J. Met.*, 1981 (November), pp. 42-47.
6. J. Szekely, N. El-Kaddah, and J.H. Grevet: in *Int. Conf. on Injection Metallurgy*, 1980, pp. 5:1-5:32.
7. J. Szekely, H.J. Wang, and K.M. Kiser: *Metall. Trans. B*, 1976, vol. 7B, pp. 287-95.
8. P.E. Anagbo and J.K. Brimacombe: *Metall. Trans. B*, 1990, vol. 21B, pp. 637-48.
9. Y.Y. Sheng and G.A. Irons: in *Process Technology Conf. (75th Steelmaking Conf.)*, L.C. Kuhn, ed., The Iron and Steel Society, Warrendale, PA, 1992, vol. 10.

10. S.T. Johansen and F. Boysan: *Metall. Trans. B*, 1988, vol. 19B, pp. 755-64.
11. S.T. Johansen, D.G.C. Robertson, K. Woje, and T.A. Engh: *Metall. Trans. B*, 1988, vol. 19B, pp. 745-54.
12. J. Szekely: *Fluid Flow Phenomena in Metals Processing*, Academic Press, New York, NY, 1979.
13. R. Kumar and N.R. Kuloor: *Adv. Chem. Eng.*, 1970 vol. 8, pp. 256-369.
14. J.F. Davidson and O.G. Schüler: *Trans. Inst. Chem. Eng.*, 1960, vol. 38, pp. 144-54.
15. T. Asaeda and J. Imberger: *J. Fluid Mech.*, 1993, vol. 249, pp. 35-57.
16. G.A. Irons and R.I.L. Guthrie: *Metall. Trans. B*, 1978, vol. 9B, pp. 101-10.
17. M. Kawakami, S. Hosono, K. Takahashi, and K. Ito: *Tetsu-to-Hagané*, 1992, vol. 78 (2), pp. 267-74.
18. P.E. Anagbo, J.K. Brimacombe, and A.E. Wraith: *Chem. Eng. Sci.*, 1991, vol. 46 (3), pp. 781-88.
19. M. Sano and K. Mori: *Trans. Jpn. Inst. Met.*, 1976, vol. 17, pp. 344-52.
20. A.H. Castillejos and J.K. Brimacombe: *Metall. Trans. B*, 1987, vol. 18B, pp. 649-58.
21. A.H. Castillejos and J.K. Brimacombe: *Metall. Trans. B*, 1987, vol. 18B, pp. 659-71.
22. I. Leibson, E.G. Holcomb, A.G. Cacoso, and J.J. Jacmic: *AIChE. J.*, 1956, vol. 2 (September), pp. 296-306.
23. R.L. Datta, D.H. Napier, and D.M. Newitt: *Trans. Inst. Chem. Eng.*, 1950, vol. 28, pp. 14-26.
24. G.C. Vliet and G. Leppert: *J. Heat Transfer, Trans. ASME*, 1961, May, pp. 163-75.
25. N. Bessho, R. Yoda, and H. Yamasaki: *Iron Steelmaker*, 1991, vol. 18 (4), pp. 39-44.
26. N. Tsukamoto, K. Ichikawa, E. Iida, A. Morita, and J. Inoue: in *74th Steelmaking Conf. Proc.*, P.A. Augius *et al.*, eds., Iron and Steel Society, Warrendale, PA, 1991, vol. 74, pp. 803-08.
27. P. Andrzejewski, K.-U. Kohler, and W. Pluschkeli: *Steel Res.*, 1992, vol. 3 (6), pp. 242-46.
28. S.L. Soo: *Fluid Dynamics of Multiphase System*, Blaisdell Publishing Co., Waltham, MA, 1967, ch. 3.
29. D.E. Hershey, B.G. Thomas, and F.M. Najjar: *Int. J. Numer. Methods Fluids*, 1993, vol. 17 (1), pp. 23-49.
30. B.G. Thomas, L.J. Mika, and F.M. Najjar: *Metall. Trans. B*, 1990, vol. 21B, pp. 387-400.
31. F.M. Najjar: Master's Thesis, University of Illinois at Urbana-Champaign, Urbana, IL, 1990.
32. B.E. Launder and D.B. Spalding: *Comp. Methods Appl. Mech. Eng.*, 1974, vol. 3, pp. 269-89.
33. X. Huang, B.G. Thomas, and F.M. Najjar: *Metall. Trans. B*, 1992, vol. 23B, pp. 339-56.
34. B.G. Thomas and F.M. Najjar: *Appl. Math. Modeling*, 1991, vol. 15, pp. 226-43.
35. X. Huang: Ph.D. Thesis, Tsinghua University, Beijing, 1988.
36. S.V. Patankar: *Numerical Heat Transfer and Fluid Flow*, McGraw-Hill, New York, NY, 1980.
37. C. Offerman: *Scand. J. Metall.*, 1981, vol. 10, pp. 25-28.
38. P. Flint: in *Proc. of 73rd Steelmaking Conf.*, Iron and Steel Society/AIME, Warrendale, PA, 1990, vol. 73, pp. 481-90.
39. B.G. Thomas, W.R. Storkman, and A. Moitra: in *Sixth Int. Iron Steel Congress*, Iron and Steel Institute of Japan, Tokyo, Japan, 1990, vol. 2, pp. 348-55.
40. X. Huang and B.G. Thomas: *Metall. Trans. B*, 1993, vol. 24B, pp. 379-93.
41. M.S. Engelman: *FIDAP Theoretical Manual—Revision 4.0*, Fluid Dynamics International, Inc., Evanston, IL, 1986.
42. R. Sussman and J. Schade: Armco Inc., Middletown, OH, private communication, 1992.
43. R. Sussman, T. Tucker, and J. Hester: Armco Inc., Middletown, OH, private communication, 1992.
44. J. Birat, M. Larrecq, J. Lamant, and J. Petegnief: in *Mold Operation for Quality and Productivity*, Iron and Steel Society, Warrendale, PA, 1991, pp. 3-14.
45. Y.H. Wang: in *Process Technology Conf. (75th Steelmaking Conf.)*, L.G. Kuhn, ed., The Iron and Steel Society, Warrendale, PA, 1992, vol. 10, pp. 271-78.
46. M. Kumada and I. Mabuchi: *Trans. Jpn. Soc. Mech. Eng.*, 1969, vol. 35, pp. 1053-61.
47. R. Gas: Inland Steel, Inc., East Chicago, IN, private communication, 1992.
48. J. Watson: Armco Research & Technology, Middletown, OH, unpublished research, 1993.
49. P.E. Liley: in *Handbook of Single-Phase Convective Heat Transfer*, S. Kakac, R.K. Shah, and W. Aung, eds., John Wiley and Sons, New York, NY, 1987, p. 22.1.
50. R.L. Powell and G.E. Childs: in *American Institute of Physics Handbook*, M.W. Zemansky, ed., McGraw-Hill, New York, NY, 1972, pp. 4-#42--4-204.
51. M. Iguchi, Z.-I. Morita, H. Tokunaga, and H. Tatemichi: *Iron Steel Inst. Jpn. Int.*, 1992, vol. 32 (7), pp. 865-72.
52. D.E. Hershey: Master's Thesis, University of Illinois at Urbana–Champaign, Urbana, IL, 1992.